BOILING HEAT TRANSFER ENHANCEMENT ON STRUCTURED SURFACES BY USING ACTIVE AND PASSIVE METHODS

by BEHNAM PARIZAD BENAM

Submitted to the Graduate School of Engineering and Natural Sciences in partial fulfillment of the requirements for the degree of Master of Science

Sabanci University
July 2022

© BEHNAM PARIZAD BENAM 2022 All Rights Reserved

ABSTRACT

BOILING HEAT TRANSFER ENHANCEMENT ON STRUCTURED SURFACES BY USING ACTIVE AND PASSIVE METHODS

BEHNAM PARIZAD BENAM

Mechatronics Engineering, M.Sc. Thesis, July 2022

Thesis Supervisors: Prof. Dr. Ali Koşar & Dr. Abdolali K. Sadaghiani

Keywords: Boiling, Heat transfer enhancement, Structured surfaces, Critical heat flux, Magnetic nanofluid, Magnetic field, Artificial cavities

Thermal management is becoming increasingly important for new electronic device applications. Boiling is a very effective phase change phenomenon capable of dissipating a large amount of heat. This thesis investigates the effect of surface structures on boiling heat transfer by using both active and passive approaches.

In the first part, comprehensive series of pool boiling tests were carried out on surfaces having microchannels with different spacings and artificial cavities to investigate the mutual effect of surface microstructures, microstructure spacing, and artificial nucleation sites on the boiling heat transfer (BHT) performance and critical heat flux (CHF). The BHT performance of different samples could be significantly improved for samples containing artificial cavities. While microchannel configurations had no significant effect at low wall superheats, further increases in wall heat flux revealed the effect of surface structure on BHT and bubble dynamics. For samples with 50 and 100 artificial cavities, the largest spacing exhibited the best performance at high heat fluxes. Furthermore, the visualization results revealed that for surfaces with artificial cavities, dry-out was the main CHF mechanism, whereas hydrodynamic instability was responsible for the occurrence of CHF for surfaces without artificial cavities, which proved the dependence of the CHF mechanism on the surface configuration.

The second part aims to experimentally investigate the effect of magnetic nanoparticles on saturated flow boiling heat transfer in a narrow microchannel by using microstructured silicon surfaces and comparing the heat transfer performance in the absence and presence of an external magnetic field. BHT results show that due to the orientation of the heating blocks, the heat transfer coefficients (HTC) on the bottom surface were higher than those on the top surface. Moreover, adding nanoparticles enhanced BHT and resulted in an increase in up to 21.5% in BHT coefficient. The presence of the external magnetic field decreases the bubble departure size and increases HTC on the top surface at high heat fluxes. The maximum HTC enhancement in the presence of a magnetic field was 25%. Bottom surface exhibited higher ferrofluid BHT enhancement in the absence of a magnetic field compared to the case with external magnetic field.

ÖZET

YAPILI YÜZEYLERDE AKTİF VE PASİF YÖNTEMLERLE KAYNAMA ISI TRANSFERI ARTIRILMASI

BEHNAM PARIZAD BENAM

Mekatronik Mühendisliği YÜKSEK LİSANS TEZİ, Temmuz 2021

Tez Danışmanı: Prof. Dr. Ali Koşar & Dr. Abdolali K. Sadaghiani

Anahtar Kelimeler: Kaynama, Isı transferi geliştirme, Yapılandırılmış yüzeyler, Kritik ısı akısı, Manyetik nanoakışkan, Manyetik alan, Yapay boşluklar

Termal yönetim, yeni nesil elektronik cihaz uygulamaları için giderek daha önemli hale gelmektedir. Kaynama, büyük miktarda ısı atma kapasitesi olan çok etkili bir faz değişimi fenomenidir. Bu tezde, hem aktif hem de pasif yaklaşımları kullanarak yüzey yapılarının kaynama ısı transferi üzerindeki etkisini araştırılmıştır.

Birinci bölümde, yüzey mikro yapılarının, mikro yapı aralığının ve yapay çekirdeklenme bölgelerinin kaynama ısı transferi (BHT) performansı üzerindeki kombine etkisini araştırmak için farklı aralıklarını ve yapay kaviteleri içeren mikro kanallara sahip yüzeyler üzerinde kapsamlı havuz kaynama testleri gerçekleştirilmiştir ve kritik ısı akısı (CHF) sonuçları elde edilmiştir. Farklı numunelerin BHT performansı, yapay kaviteteleri içeren numuneler için önemli ölçüde iyileştirilmiştir. Mikrokanal konfigürasyonları, düşük duvar kızma sıcaklıklarında önemli bir etkiye sahip değilken, duvar ısı akısındaki daha fazla artış, yüzey yapısının BHT ve kabarcık dinamiği üzerindeki etkisini ortaya çıkarmıştır. 50 ve 100 yapay kaviteli numuneler için en büyük mesafe, yüksek ısı akılarında en iyi performansı sergilemiştir. Ayrıca, görselleştirme sonuçları, yapay kaviteli yüzeyler için ana CHF mekanizmasının kuruma olduğunu, yapay kaviteleri olmayan yüzeyler için CHF'nin oluşumundan hidrodinamik kararsızlığın sorumlu olduğunu ortaya koymuş, bu da CHF mekanizmasının yüzey konfigürasyonuna bağımlılığını kanıtlamıştır.

İkinci kısım, mikro yapılı silikon yüzeyler kullanarak dar bir mikrokanalda manyetik nanoparçacıkların doymuş akış kaynama ısı transferi üzerindeki etkisini deneysel olarak araştırmayı ve harici bir manyetik alan yokluğunda ve varlığında ısı transfer performansını karşılaştırmayı amaçlamaktadır. BHT sonuçları, ısıtma bloklarının oryantasyonu nedeniyle, alt yüzeydeki ısı transfer katsayılarının (HTC) üst yüzeydekilerden daha yüksek olduğunu göstermiştir. Ayrıca, nanopartiküllerin varlığı BHT'yi iyileştirmiş ve BHT katsayısında %21.5'e varan bir artış sağlamıştır. Dış manyetik alanın varlığı, kabarcık ayrılma boyutunu azaltmış ve yüksek ısı akılarında HTC'yi artırmıştır. Manyetik alan varlığında maksimum HTC artışı %25 olmuştur. Alt yüzey için harici manyetik alan ile karşılaştırıldığında bir manyetik alan yokluğunda ferrofluid BHT artışı daha fazla olmuştur.

ACKNOWLEDGMENTS

Firstly, I would like to thank my thesis supervisors, Prof. Dr. Ali Koşar and Dr. Abdolali K. Sadaghiani, for offering me this great opportunity to learn and for their guidance, patience, and endless support. I do not think it is an exaggeration to say that our world needs these types of people more than it ever has before, and I consider myself very fortunate to have been able to fully benefit from the emotional and motivational support they have provided.

I need to thank Assoc. Prof. Dr. Feray Bakan Misirlioğlu and Prof. Dr. Yegân Erdem my honorable jury members, for their dedication and constructive comments for improving the technical context of the thesis and make this thesis more professional.

This work was supported by TUBITAK (The Scientific and Technological Research Council of Turkey) Support Program for Scientific and Technological Research Project (Grant No. 119N116). Equipment utilization support from the Sabanci University Nanotechnology Research and Applications Center (SUNUM) is gratefully appreciated.

Special thanks to all of my dear friends at Sabanci University who have become more to me than just friends throughout the duration of these past years and supported me along the way during my study at Sabanci.

I would like to thank my beloved family for all the inspiration, unconditional support throughout my lifetime. They have always encouraged me to follow my dreams. Without them, this journey would not be possible for me.

Finally, and most importantly, I would like to express my infinite gratitude to my everlasting love and my best friend, Darya Farrokhnemoun, for her love, unwavering support, and encouragement throughout my academic journey career and life. I owe you everything.



TABLE OF CONTENTS

LIST OF TABLESii	i
LIST OF FIGURESir	V
Chapter 1. Introduction	1
1.1 Introduction- A parametric study on pool boiling heat transfer and critical heat flux on structured surfaces with artificial cavities	1
1.2 Introduction- On saturated flow boiling heat transfer of deionized water and magnetic nanofluid on structured surfaces with and without external magnetic field 3	
1.3 Structure of thesis	5
Chapter 2. A parametric study on pool boiling heat transfer and critical heat flu on structured surfaces with artificial cavities	
2.1 Experiments	7
2.1.1 Experimental setup and procedure	7
2.1.2 Sample preparation and characterization	9
2.1.3 Data reduction and analysis	1
2.2 Result and discussion	3
2.2.1 The effect of the number of artificial cavities	4
2.2.2 The effect of microchannel spacing	6
2.2.2.1 Samples without artificial cavities	6
2.2.2.2 Samples with medium density of artificial cavities	8
2.2.2.3 Samples with high density of artificial cavities	0
2.2.3 Critical heat flux (CHF)	2
Chapter 3. On saturated flow boiling heat transfer of deionized water and magnetic nanofluid on structured surfaces with and without external magnetic field 2	
3.1 Bubble force analyses	6
3.1.1 Surface tension force	7
3.1.2 Shear lift force	7
3.1.3 Unsteady drag force	8
3.1.4 Buoyancy, contact pressure, hydrodynamic, and quasi-steady drag	
forces	8
3.1.5 Presence of a magnetic field	9

3.2	Experiments	. 30
	3.2.1 Experimental setup and procedure	. 30
	3.2.2 Ferrofluid and magnetic field characterization	. 32
	3.2.2.1 Ferrofluid preparation	. 32
	3.2.2.2 Magnetic field characterization	. 33
	3.2.3 Sample preparation and characterization	. 36
	3.2.4 Data reduction and Uncertainties	. 38
3.3	Results and discussion	40
	3.3.1 Validation	40
	3.3.2 Test with DI water (DW)	. 42
	3.3.3 Test with ferrofluid (FF)	. 43
	3.3.4 Test with ferrofluid and magnetic field (FF/MF)	. 44
	3.3.5 Heat transfer results	. 45
Chapter 4.	Conclusion and Future Works	47
	Conclusion- A parametric study on pool boiling heat transfer and critical leat flux on structured surfaces with artificial cavities	. 47
n	Conclusion- On saturated flow boiling heat transfer of deionized water and nagnetic nanofluid on structured surfaces with and without external magnetical 48	
4.3	Future Works	49

LIST OF TABLES

Table 1. Tested samples and their physical characteristics. For all tes	ted samples
L_1 =10mm and L_2 =8mm	10
Table 2. Uncertainties in major parameters.	13
Table 3. Definition of heat flux from Low to High.	15
Table 4. Helmholtz coil characteristics	34
Table 5. Measured values of the magnetic field intensity and calculat	ed values 36
Table 6. Uncertainties in experimental parameters.	40

LIST OF FIGURES

Figure 1. Schematic of the pool boiling experimental setup. a) in-house boiling
heat transfer apparatus utilized for pool boiling experiments, b) pool boiling test section,
which consists of 1) condenser, 2) immersed heater, 3) thermocouples, 4) plexiglass, 5)
sample, 6) heating block, 7) cartridge heaters, 8) temperature measurement holes, 9)
Teflon block for insulation. 8
Figure 2. Fabrication process flow of prepared samples
Figure 3. Silicon wafer sizes and configuration
Figure 4. SEM images of the tested samples
Figure 5. Wall temperature measurement locations and data reduction approach
Figure 6. Boiling curves for present experimental research and literature studies.
Figure 7. Boiling curves for tested samples
Figure 8. Boiling curves for different samples. The microchannel spacing for
each of these samples is: (a) 20 μ m (b) 40 μ m (c) 50 μ m (d) 80 μ m
Figure 9. Effect of artificial cavities for different surfaces at heat flux 7.2
(W/cm ²) for surfaces #1, and #3 (<i>Table 1</i>)
Figure 10. Comparison in heat transfer coefficient (HTC) for different surfaces
with same spacing and different number of artificial cavities
Figure 11. Different samples with different spacings and without artificial
cavities. (a) heat flux $7.2(W/cm^2)$, (b) heat flux $45(W/cm^2)$, (c) heat flux $115(W/cm^2)$. 18
Figure 12. Different samples with different spacings and with 50 numbers of
artificial cavities. (a) heat flux 7.2(W/cm ²), (b) heat flux 45(W/cm ²), (c) heat flux
115(W/cm ²)
Figure 13. Different samples with different spacings and with 100 numbers of
artificial cavities. (a) heat flux 7.2(W/cm ²), (b) heat flux 45(W/cm ²), (c) heat flux
115(W/cm ²)
Figure 14. Heat transfer coefficient as a function of heat flux for a) samples
without artificial cavities, b) samples with medium density of cavities c) samples with
high density of cavities.

Figure 15. Schematic of the Zuber hydrodynamic instability model: (a) Vapor jet
formation prior to CHF. (b) Vapor stem growth. (c) Vapor blanket formation due to
Helmholtz instability. Adopted version from Liang and Mudawar [91]23
Figure 16. Vapor blanket formation due to hydrodynamic instability in surface
#10 at CHF point (165.7 (W/cm ²))
Figure 17. Schematic of Haramura and Katto's microlayer dry-out model 24
Figure 18. Vapor blanket formation and departure due to dry-out mechanism on
sample #3 at CHF point (181 (W/cm ²)). (Red indicators show small bubbles)
Figure 19. Effect of channel spacing and artificial cavities on the CHF for all the
surfaces
Figure 20. Force balance of a vapor bubble at a nucleation site
Figure 21. Flow boiling test section design: (a) fabricated test section, (b)
exploded view and different parts of the test section, (c) microchannel schematic and
place of the heating surfaces
Figure 22. Schematic of the experimental setup for flow boiling tests
Figure 23. Using Helmholtz coils as an external magnetic field around the test
section. The distance between two coils is 150mm, and the diameter of each coil is
300mm
Figure 24. Two different types of nanofluids
Figure 25. Different dilutions of nanofluids
Figure 26. Different dilutions (a) after mixing (b) after one day (c) after one
week (1: LA 0.01%, 2: LA 0.02%, 3: PAA 0.02%)
Figure 27. Helmholtz coils produce an external magnetic field
Figure 28. Magnetic field intensity of each coil and the overall value of the
magnetic field at different locations [100]
Figure 29. Structured surfaces with different cavity patterns, (a) square,
(b)circular
Figure 30. The fabrication process for structured surfaces. a)Silicon substrate,
b)Al metal layer as a mask, c)Spin coated PR, d)Patterned PR by lithography,
e)Patterned Al later by wet etching, f)PR washed away, g)Etching Silicon, h)Patterned
surface after removing Al layer
Figure 31. (a) Silicon wafer mask design for different pitch sizes, (b) Diced
silicon wafer
Figure 32. Contact angle of the channel wall made of polycarbonate
v

Figure 33. Schematic of thermocouple locations and approach (thermal
resistance network) to calculate the surface temperature
Figure 34. Validation of experimental results
Figure 35. Boiling images at different heat fluxes and constant mass flux
(G=300(Kg/m²s)). a) low heat flux, b) medium heat flux, c) high heat flux, d) dry-out
for the topside heating surface, and bubbles which still generated from the bottom
surface. 43
Figure 36. a) Boiling curves b) Heat transfer coefficients for the cases of heating
blocks on top and bottom sides for ferrofluid
Figure 37. Ferrofluid boiling images without external magnetic field at different
heat fluxes and constant mass flux ($G=300(kg/m^2s)$). a) low heat flux, b) medium heat
flux, c) high heat flux, d) dry-out for the top surface
Figure 38. a) Boiling curves b) Heat transfer coefficients for the cases of heating
block on top and bottom sides for ferrofluid without external magnetic field effect. \dots 44
Figure 39. Ferrofluid boiling images in the presence of an external magnetic
field effect (3.7 (mT)) at different heat fluxes and constant mass flux (G=300(kg/m^2s)).
a) low heat flux, b) medium heat flux, c) high heat flux, d) dry-out on the top surface. 44
Figure 40. a) Boiling curves b) heat transfer coefficients of top and bottom
surfaces for the ferrofluid case in the presence of external magnetic field
Figure 41. Boiling curves for different conditions a) bottom surface, b) top
surface (G=300 (Kg/ m^2 s))
Figure 42. Heat transfer coefficients profiles for a) bottom surface and b) top
surface
Figure 43. SEM images of silicon surface with square cavities a) before the test,
b) tested with ferrofluid) tested with ferrofluid and external magnetic field effect 46

Chapter 1. Introduction

1.1 Introduction- A parametric study on pool boiling heat transfer and critical heat flux on structured surfaces with artificial cavities

Heat generation in new generation electronic devices has become a serious problem like thermal management for high power for the effective performance of device over the last few decades. Thermal management of such electronic systems requires efficient heat dissipation to ensure their safe and reliable operational conditions. Boiling is a highly effective phase change heat transfer mechanism dissipating a significant amount of heat through sensible and latent heat [1–8]. The boiling heat transfer (BHT) performance is characterized by heat transfer coefficient (HTC) and critical heat flux (CHF). Many studies have been performed to enhance the boiling performance by increasing HTC and extending CHF [9–13]. One of the mostly used approaches is surface modification by external coating [10,14,15] or integral structuring [16–19]. The surface textures generally consist of micro pin fins [20-24], microchannels [3,25-28], and artificial cavities [29–37]. The above-mentioned techniques utilize specific surface features to manipulate the bubble nucleation, growth, and departure processes as well as surface rewetting and liquid replenishment. As an example, McHale and Garimella [38,39] showed that micro/nanostructures on the surfaces increased the number of active nucleation sites in pool boiling studies. During nucleate boiling, the cavities are potential locations to trap the vapor, increase bubble nucleation sites and enhance pool boiling heat transfer [40]. In another study, Dong et al. [41] examined the surface microstructure and wettability effect on heterogeneous nucleation in pool boiling by considering the Gibbs free energy and availability approaches. They also investigated the bubble dynamics behavior from the microstructures by presenting the nucleation site density and departure frequency [42] one of the critical parameters influencing BHT. The open microchannels or rectangular micro fins could enhance heat transfer by inducing the capillary flow and separating the escaping vapor and replenishment liquid [43–45]. As an example, Li et al. [46] conducted pool boiling experiments on copper surfaces with circular-shaped cavities. The bubble escaping resistance was decreased by increasing the cavity number and diameter, which resulted in higher HTC at high heat fluxes. However, when the number and diameter were too large, there was a deteriorating trend due to the decrease in heat transfer area and capillary force.

The interface area between the vapor and heated surface determines the bubble size. Depending on this size, the vapor phase becomes either stable or unstable on the heater surface. If the wall superheats are low, the isolated bubbles grow and depart from the superheated surface. However, by increasing the wall temperature, the bubbles nucleating from nearby sites coalescence to each other and might form giant bubbles [6]. As an example, Yu et al. [31,47] investigated pool boiling of FC-72 on surfaces with rectangular fins and artificial cavities and reported that the cavity density influenced HTC and CHF, and vapor/bubble coalescence occurred at high heat fluxes rather than at low heat fluxes. Zhang and Shoji [30] explored the nucleation site interaction in pool boiling and underlined three effective parameters: hydrodynamic interaction among bubbles, thermal interaction between nucleation sites, and horizontal and declining bubble coalescence. Some articles reported that by increasing the active nucleation sites for surfaces with nanotubes at low heat fluxes, the bubble departure diameter decreases and departure frequency increases. Zupancic et al. [48] also obtained similar results for biphilic surfaces regarding active nucleation sites.

The other important parameter is the cavity spacing [5]. In an experimental study, Chatpun et al. [49] revealed that cavity spacing had an influence on the bubble characteristics such as bubble departure frequency, bubble departure diameter, temperature distribution on the heated surface, and heat transfer characteristics. Nikulin et al. [50] showed that HTC and bubble behavior were not affected by the large spacing, which was significantly longer than the bubble departure diameter. The spacings on the order of the bubble departure diameter, on the other hand, triggered the generation of slug flow in the bundle, which was highly advantageous for heat exchange at low heat fluxes. Finally, in tube bundles with small length to diameter ratios, narrow spacings being significantly shorter than the bubble departure diameter demonstrated the ability to improve boiling heat transfer.

While various research groups reported the effect of the microstructures on HTC and CHF, the number of comprehensive parametric studies on the mutual effect of surface structures and artificial cavity on CHF mechanisms is considerably limited. Also, there is still a need to investigate combined interactions of the nucleation sites and bubble dynamics to better understanding different structured surfaces behavior on BHT. For covering this issue in this thesis, the fabricated surfaces with the MEMS (microelectromechanical systems) technology, which include rectangular fins (microchannels), circular cavities, and a combination of both of them, were employed to enhance active nucleation sites and to modify surface wettability. The effects of the microchannel width and number, circular cavity diameter and spacing were explored in pool boiling experiments. In addition, visualization studies were also performed with a high-speed camera to reveal the characteristics of BHT, CHF, and bubble dynamics. Eventually, the designed surfaces were compared with each other to present an optimum surface configuration.

1.2 Introduction- On saturated flow boiling heat transfer of deionized water and magnetic nanofluid on structured surfaces with and without external magnetic field

Flow Energy saving and energy efficiency improvement are of cardinal important in addressing the global energy crisis. In this regard, heat transfer enhancement is an efficient approach to save energy and achieve a higher energy efficiency [51,52]. There are several techniques to achieve effective heat transfer. BHT is one of the most popular and widely used ones. There are many industrial applications of BHT including air conditioning, refrigeration, nuclear reactors, chemical engineering, aircraft and spacecraft thermal management [53]. In order to make the processes in these applications more energy-efficient, BHT must be improved. This is also necessary for significantly reducing the energy consumption and system size and volume.

It is possible to categorize the methods for improving BHT into two broad categories: active and passive methods [14,54,55]. Passive methods rely on fluid and the surface characteristics [52,56–58], whereas active methods utilize external power and field to improve heat transfer [59,60]. Systems involving can benefit from the application of external fields such as magnetic and electric fields, which can be easily generated during the process and thus be used as active heat transfer enhancement.

Magnetic fluids, also known as ferrofluids, have been one of the primary research topic in nanotechnology due to their applications in magnetic sealing, electronic

packaging, dynamic loudspeakers, electronic packaging, aerospace, biotechnology, microfluidics, and drug delivery [61–66]. Magnetic nanoparticles utilized in magnetic fluids are often made of metals (ferromagnetic materials) such as iron, nickel, and cobalt, as well as their oxides such as spinel-type ferrites magnetite (Fe₃O₄) in various sizes and shapes. In addition to ameliorating thermal characteristics, they also have outstanding magnetic properties and thermophysical properties similar to other working fluids. Therefore, magnetic fields could be applied to manipulate their flow, heat transfer, and movement, which paves way to their potential for their use in different fields [67–72].

There are already some studies on magnetically actuated nanoparticles to improve heat transfer and overall system stability. Although the thermal conductivity of nanoparticles is higher than that of deionized water, some studies reported a decrease in the HTC, an improvement in BHT was observed in some studies. For example, under boiling conditions, Şeşen et al. [73] investigated the heat transfer properties of magnetically actuated nanofluids (Fe3O4), and the two-phase average HTC for the magnetic actuation case in boiling increased by 17%. Moreover, magnetically activated nanoparticles slowed nanoparticle cluster formation and its surface deposition. In another study, Sarafraz et al. [74] investigated the effect of flow rate, inlet subcooling, heat flux, and mixture concentration on HTC in subcooled BHT of water/diethylene glycol. Their results showed that increasing the mixture concentration increased the flow boiling heat transfer coefficient up to a certain level of volumetric concentrations, more than 5%, beyond which HTC decreased. Zonouzi et al. [75] explored the effects of a quadrupole magnetic field on the hydrodynamics and heat transfer of water/Fe₃O₄ in a vertical tube. Since the magnetic field within the tube was radial, the magnetic fluid was pushed away from the heated wall by the magnetic force. They also observed that an increase in the axial distance of the quadrilateral magnets from the tube inlet increased the maximum value of local HTC. Lajvardi et al. [76] investigated laminar flow of Fe3O4 nanoparticles (10 nm) and water in a heated tube. Due to the sheer influence of the applied magnetic field and the percentage of magnetic nanoparticles, the HTC improved. Guo et al. [77,78] performed numerical simulations on the influence of magnetic fields on boiling of magnetic fluids and obtained an improvement in heat transfer with an increase in the magnetic field. In another study, Arya et al. [79] concluded that the presence of a magnetic field causes a reduction in nanoparticle deposition rate in pool boiling, resulting in decreased thermal resistance and less deposition, while HTC decreased less with the test

duration during experiments with Fe3O4/deionized water fluids. In addition to increasing surface resistance, the lack of a magnetic field also suppressed bubble generation. Aminfar et al. [80] performed numerical simulations to investigate ferrofluid flow and heat transfer in a rectangular channel in the presence of a non-uniform magnetic field. Applied magnetic field increased the Nusselt number and friction factor and generated a pair of vortices, which augmented heat transfer and prevented nanoparticle sedimentation. Ghofrani et al. [81] studied forced convective heat transfer of a ferrofluid moving within a copper tube under alternating and constant magnetic fields. They observed that a constant magnetic field had no effect on heat transfer.

By considering all the above-mentioned studies, it can be deduced that rigorous research efforts on boiling of magnetic fluids have been made. However, few studies have focused on the visualization and analysis of the combination of significant parameters, while there are even fewer studies on flow boiling of magnetic fluids. In this thesis, the combined effect of Superparamagnetic Iron Oxide Nanoparticles (SPION) inside the working fluid water in the existence and absence an external magnetic field and structured surface with square and circular cavities, which was prepared with the implementation of the MEMS (microelectromechanical systems) technology, on flow boiling was investigated. In addition, a complementary visualization study was conducted on a rectangular minichannel with the use of magnetically actuated nanoparticle in order to better understand bubble dynamics and BHT trends under different experimental conditions.

1.3 Structure of thesis

In the current dissertation, two different boiling types, including pool boiling and flow boiling, were investigated in the following chapters:

• Chapter 2: Investigating pool boiling heat transfer and critical heat flux on different structured surfaces. These structured surfaces were designed with the MEMS technology and include different microchannel spacing and cavities. By changing the cavities number and spacing of microchannels, BHT, HTC, and CHF also changed. A detailed explanation including experimental setup and procedure, data reduction and analysis, sample preparation and characterization, and results with a discussion about them were covered in this chapter.

- Chapter 3: Experimental study was performed on flow boiling heat transfer on structured surfaces with different working fluids, including DI water and magnetic nanofluid, on structured surfaces in the presence and absence of an external magnetic field. This chapter covers all the related topics including bubble force analyses, experimental setup and procedure, nanofluid and magnetic field preparation and characterization, sample preparation and characterization, data reduction and uncertainties, and results with comprehensive discussion.
- Chapter 4: This chapter includes major conclusions of the presented works and recommendations for future research directions.

Chapter 2. A parametric study on pool boiling heat transfer and critical heat flux on structured surfaces with artificial cavities

2.1 Experiments

2.1.1 Experimental setup and procedure

Figure 1.a shows the in-house boiling heat transfer apparatus utilized for pool boiling experiments, and Figure 1.b shows an exploded view of the pool boiling test section, which consists of 1) condenser, 2) immersed heater, 3) thermocouples, 4) plexiglass, 5) sample, 6) heating block, 7) cartridge heaters, 8) temperature measurement holes, 9) Teflon block for insulation. Degassed deionized water (DI) was used as the working fluid. Silicon wafers with a thickness of 600 (µm), thermal conductivity of 130 (W/m.K), dimensions of 12.5 x 12.5 (mm²), and surface roughness of 0.145 nm were used as the test samples. Aluminum was chosen as the heating block material because of its high thermal conductivity and machinability. An immersion heater was used to maintain the desired fluid temperature (saturation temperature) at atmospheric pressure. Four vertical cartridge heaters were used to provide heat to the test section via a DC power source. Surface measurements were taken with horizontal thermocouples (placed 2 mm below the tested samples), whereas heat flux calculations were done with vertical thermocouples (1-D conduction). A glass pool was used to visualize the boiling process. The outside and inner dimensions of the glass pool were 60 x 60 x 50 (mm³) and 40 x 40 x 50 (mm³), respectively. In the pool, a thermocouple (for temperature measurement) and a submerged heater (to maintain the saturated condition) were installed. The amount of working fluid was kept constant during the tests by employing a vertical condenser open to ambient pressure. The aluminum heating part was insulated with a Teflon block to reduce heat losses. To be able to connect all of the pieces together, a sandwich mechanism

was used. All of the data was collected under steady state conditions. CHF represented the heat flux, at which a small increase in heat flux (around 1%) resulted in a high surface temperature rise (more than 20 °C) and a thick vapor layer covering the heating surface.

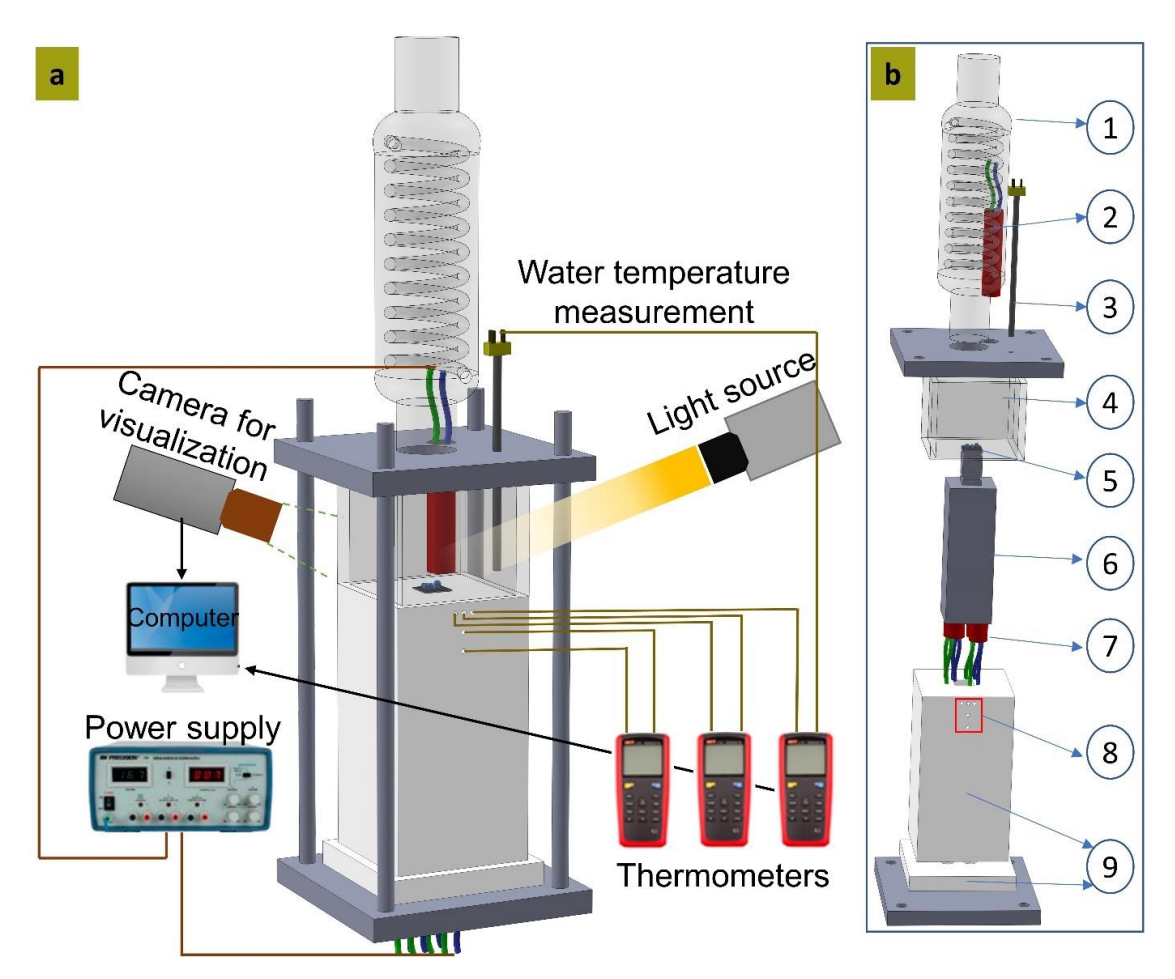


Figure 1. Schematic of the pool boiling experimental setup. a) in-house boiling heat transfer apparatus utilized for pool boiling experiments, b) pool boiling test section, which consists of 1) condenser, 2) immersed heater, 3) thermocouples, 4) plexiglass, 5) sample, 6) heating block, 7) cartridge heaters, 8) temperature measurement holes, 9) Teflon block for insulation.

2.1.2 Sample preparation and characterization

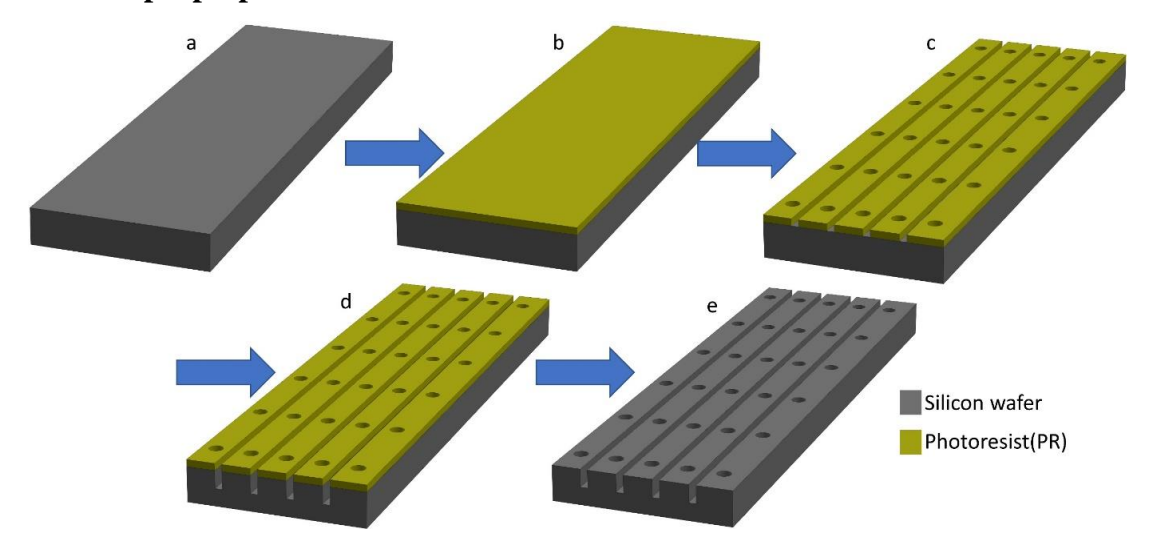


Figure 2. Fabrication process flow of prepared samples.

Figure 2 illustrates the process flow of fabricated samples. Accordingly, first, the 4-inch silicon wafer with a thickness of 500 µm (University Wafer, Inc., Boston, MA, USA) was cleaned with acetone, isopropanol, and was dried by nitrogen gas. Then, using a spin coater, the (AZ 4562) photoresist (Microchemicals Corp.) was coated for 45 seconds at 4000 rpm with a 600 rpm/s angular acceleration. The wafer was then heated at 115°C for 90 seconds in the soft bake procedure to improve sample and photoresist bonding. After that, the coated silicon wafer was exposed to UV light using a Mask Aligner UV-Lithography device (Midas System Co., Ltd., Daejeon, Korea, MDA-60MS Mask Aligner 4") through the photomasks with arrays of micro-holes printed on acetate. Following that, the sample was submerged in the developer, a 1:3 mixture of AZ 400K (Microchemicals Corp.) and DI water, for two minutes to remove the exposed region. Before starting with the etching procedure, the substrate was heated for five minutes on a hot plate at 110°C. **Table 1** includes the geometry of fabricated samples. Their depths were set at about 50 µm. Deep reactive ion etching (DRIE) is a type of dry etching used for structures with high aspect ratios (mostly silicon) and a depth of hundreds of microns [82]. This technique, known as the Bosch process, has two basic steps: etching and deposition. The reactive gas used in the etching stage was SF₆. The silicon was predominantly etched vertically by the Fluorine plasma (F+). The C₄F₈ gas was used in the deposition process to create a fluoropolymer passivation layer that prevents lateral etching [83]. Then, the substrate was diced into pieces $(15 \times 15 \text{ mm}^2)$ to be used in pool boiling experiments **Figure 3**. The SEM images of fabricated samples are shown in Figure 4.

 $Table\ 1.\ Tested\ samples\ and\ their\ physical\ characteristics.\ For\ all\ tested\ samples\ L_1=10mm\ and\ L_2=8mm$

Sample #	W_1 (μ m)	W_2 (μ m)	S (µm)	D (µm)	# Of cavities	Sample name
1	100	80	20	-	-	S20-D0-#0
2	100	80	20	40	50	S20-D40-#50
3	100	80	20	40	100	S20-D40-#100
4	100	60	40	-	-	S40-D0-#0
5	100	60	40	30	50	S40-D30-#50
6	100	60	40	30	100	S40-D30-#100
7	100	50	50	-	-	S50-D0-#0
8	100	50	50	25	50	S50-D25-#50
9	100	50	50	25	100	S50-D25-#100
10	100	20	80	-	-	S80-D0-#0
11	100	20	80	10	50	S80-D10-#50
12	100	20	80	10	100	S80-D10-#100

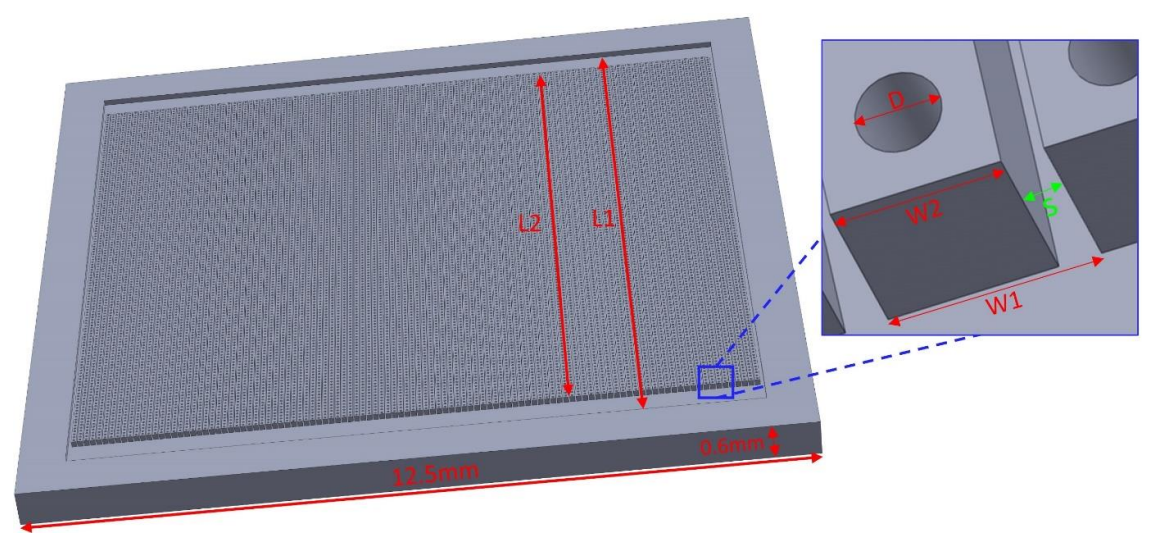


Figure 3. Silicon wafer sizes and configuration.

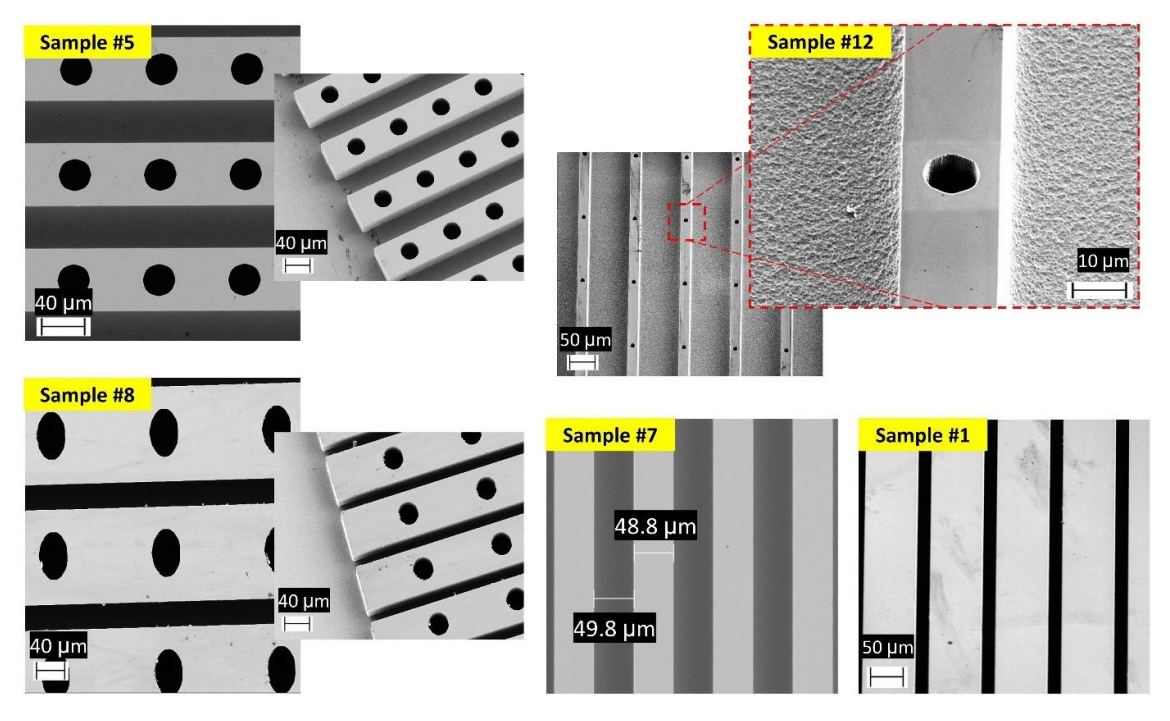


Figure 4. SEM images of the tested samples.

2.1.3 Data reduction and analysis

The heat transfer parameters including heat flux, wall superheat, and heat transfer coefficient were calculated using temperature measurements from the wall surface, voltage, and current values of the DC power supply. The following equation was used to calculate the net heat flux:

$$\dot{Q} = \frac{VI - Q_{loss}}{A} \tag{2-1}$$

where V and I are the voltage and current, respectively, Q_{loss} is the heat loss, and A is the heated surface area. In boiling experiments, heat losses were calculated as the difference between the input power and the amount of cooling energy in single phase flow regime. A Teflon block, a common insulator, covered the aluminum heating part to reduce heat loss. A natural convection analysis was used to calculate the amount of heat loss at each heat flux. As a result, the heat losses were found to be between 5% and 10%. The following equation was used to calculate the boiling heat transfer coefficient, h:

$$h = \frac{\dot{Q}}{T_{vv} - T_{ext}} \tag{2-2}$$

Here \dot{Q} is the wall heat flux, T_w the wall temperature, and T_{sat} the saturation temperature at the local liquid pressure. The wall superheat (ΔT_{sat}) is defined as the difference between the saturation temperature (T_{sat}) and the average surface temperature $T_w =$

 $\sum_{1}^{3} T_{w,i}/3$, defined as the average of three thermocouples located under the heating surface. The average of the thermocouple measurements (T_{th}) and the thermal resistance from the thermocouple to the surface (R_c) were used to calculate the wall temperatures:

$$T_{w,i} = T_{th,i} - (\dot{Q} \times R_c) \tag{2-3}$$

The thermal resistance between the thermocouples and surface is R_c , as shown in **Figure** 5, is stated as:

$$R_c \times A = \frac{L_1}{K_{AL}} + R_{T.P} + \frac{L_2}{K_{Si}}$$
 (2-4)

where A is the cross-sectional area (here $12.5 \times 12.5 \text{ mm}^2$), L_1 is the distance between the thermocouples and surface, and L_2 is the silicon surface thickness. In addition, the conductivities of the aluminum and silicon surfaces are represented by K_{AL} and K_{Si} , respectively. $R_{T.P}$, the resistance of the thermal paste between the surface and the heating block, of 6×10^{-6} (m²K/W) from the manufacturer's datasheet is used.

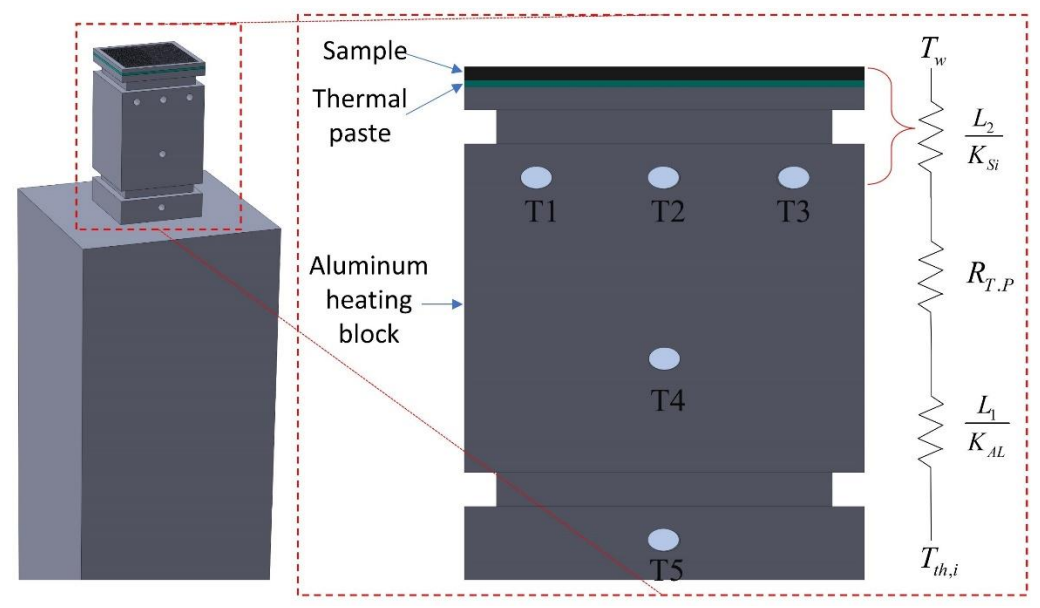


Figure 5. Wall temperature measurement locations and data reduction approach

Each experiment was repeated for three times to ensure the repeatability of the results. The uncertainty propagation method was used to calculate the uncertainties in experimental parameters [84].

Table 2 shows the uncertainties in major parameters.

Table 2. Uncertainties in major parameters.

Parameters	Uncertainties		
Voltage	±1 (V)		
Current	$\pm 0.1 (A)$		
Image pixel size	250 (µm)		
Wall temperature	±1 (°C)		
Fluid temperature	±0.5 (°C)		
Critical heat flux (CHF)	$\pm 3\%$ (W/cm ²)		
Heat transfer coefficient	±4.5-7% (W/m². K)		

2.2 Result and discussion

This study focuses on the effect of artificial inter-cavity number and spacing and microchannel spacing on the nucleate boiling performance, bubble nucleation parameters, and CHF for a test surface with micro-circular cavities immersed in saturated water at atmospheric pressure.

In order to validate experimental results, the findings of pool boiling curves for deionized water and bare silicon surface were compared with experimental studies reported in the literature, such as Motezakker et al.[7], Cho et al. [85], and KC et al. [86]. As shown in **Figure 6**, the experimental results were in good agreement with previous pool boiling curve research.

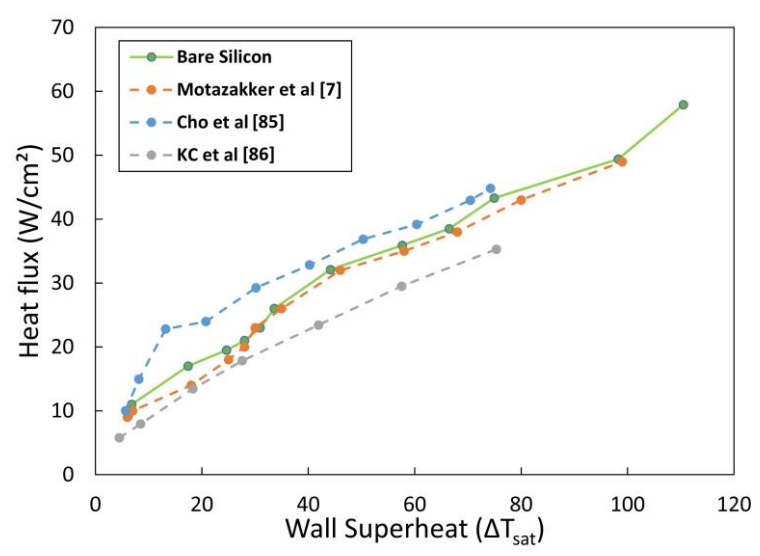


Figure 6. Boiling curves for present experimental research and literature studies.

The nucleate boiling performance was determined by evaluating the pool boiling curves for structured and plain surfaces. Cavities on the heated structured surface act as nucleation sites, thereby reducing the boiling inception superheat. The present study comprises 12 different silicon surfaces with different geometric parameters listed in **Table 1**. Boiling curves for different surfaces are included in **Figure 7** as a single graph for providing a better comparison.

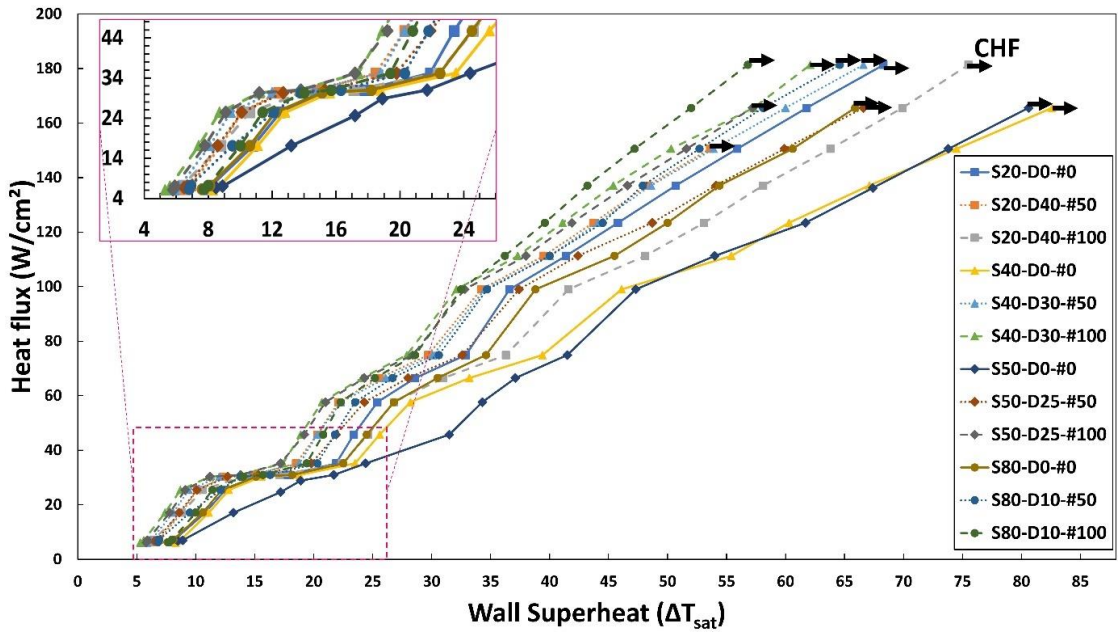


Figure 7. Boiling curves for tested samples.

2.2.1 The effect of the number of artificial cavities

Samples with different geometrical properties having 0, 50, and 100 artificial cavities were tested to investigate the effect of the number of nucleation sites and to study the combined effect of the surface structure and artificial cavities on the Onset Nucleate Boiling (ONB) and bubble dynamics. **Figure 8** compares the boiling curves for samples with the same microchannel spacing and different nucleation sites. As expected, at a fixed microchannel spacing, wall superheat decreases with the number of artificial cavities on the superheated surface. As reported in the study of Zhong et al. [29], artificial cavities act as nucleation sites and enhance the bubble nucleation process and reduce the required wall superheat for ONB. Furthermore, by looking at profiles corresponding to different spacings, except samples with S=20 µm at low heat fluxes, it can be observed that the effect of microchannel spacing is dominant over the number of cavities for S=20 µm as depicted in **Figure 8a**. For samples with S=20 µm at low heat fluxes by increasing number of cavities BHT is also enhanced. Boiling images also support these findings, as seen in **Figure 9**. Accordingly, it is obvious when the number of cavities increases, there exist

more nucleation points and more bubbles, which assist in reducing the wall superheat and enhancing BHT. From Figure 7 (b-d), it is evident that in the samples S40, S60 and S80, the effect of the cavity number is obvious as BHT increases with the number of cavities. However, for samples S20 with the smallest spacing (length of spacing is half of the cavities diameter), the formation of nucleation points in the cavities is prevented, and the distance between the micro-channels spacing serves as nucleation points, which does not allow for the generation of nucleation points in the cavities anymore. Therefore, with an increase in the number of cavities, the sample contact surface with the fluid decreases and partially limits the enhancement of the surface performance in this group. The obtained results also indicate that while the microchannel configurations have no considerable effect at low heat flux (defined in **Table 3**), further increasing the heat flux reveals the surface structure effect on BHT and bubble dynamics.

Table 3. Definition of heat flux from Low to High.

Heat flux definition	Heat flux range (W/cm ²)
Low	0-40
Medium	40-100
High	100-200

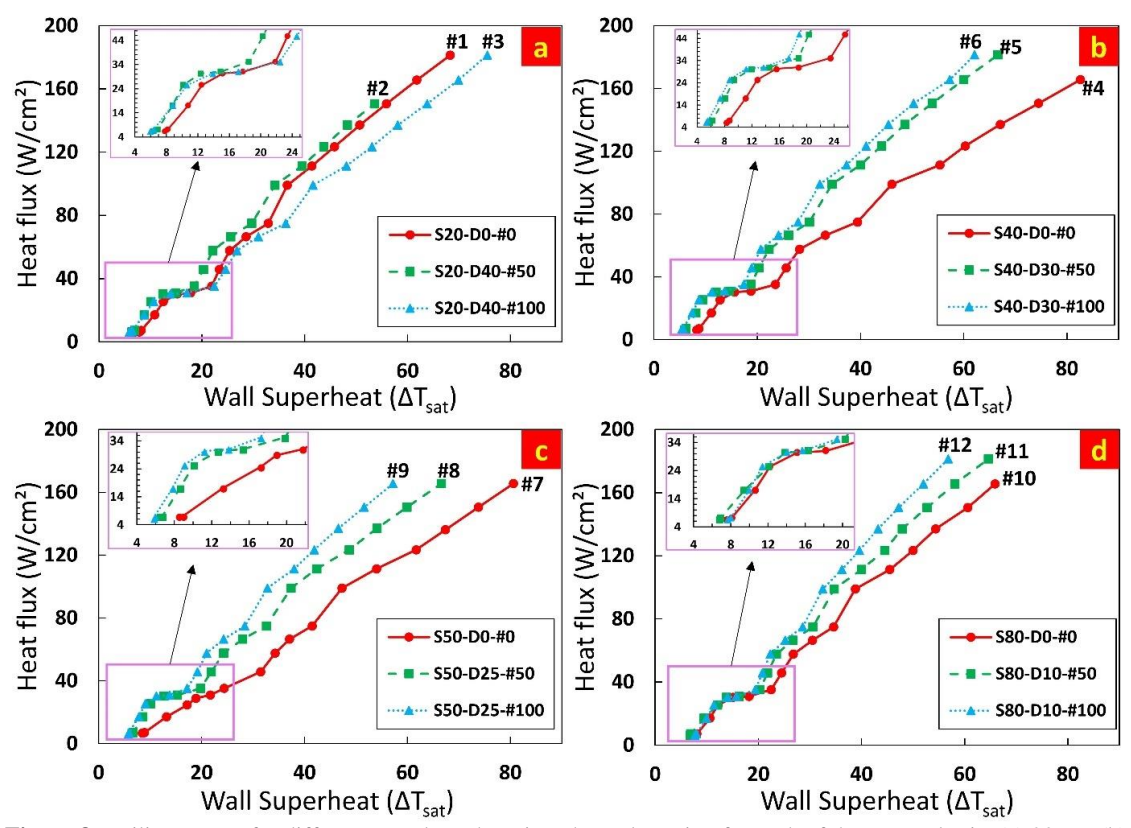


Figure 8. Boiling curves for different samples. The microchannel spacing for each of these samples is: (a) 20 μ m (b) 40 μ m (c) 50 μ m (d) 80 μ m.

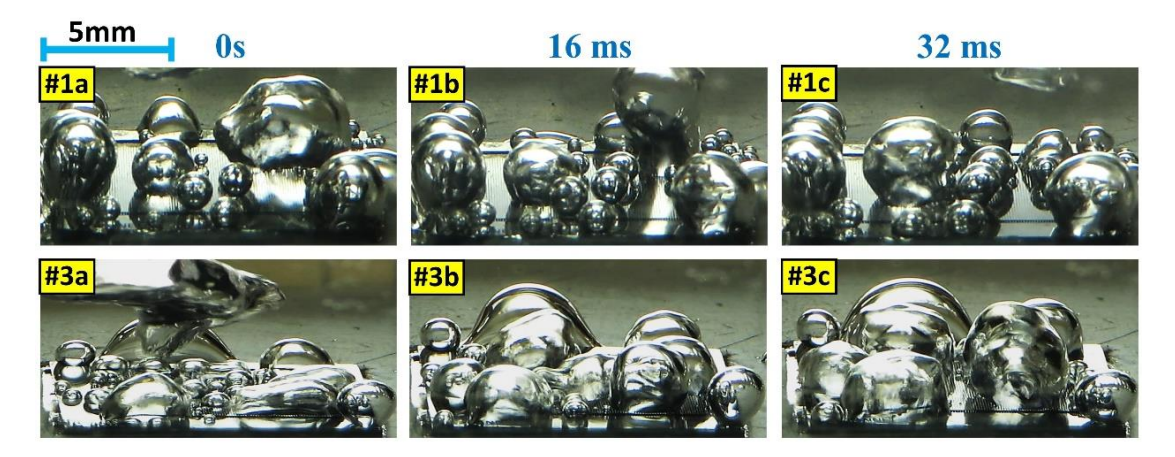


Figure 9. Effect of artificial cavities for different surfaces at heat flux 7.2 (W/cm²) for surfaces #1, and #3 (Table 1).

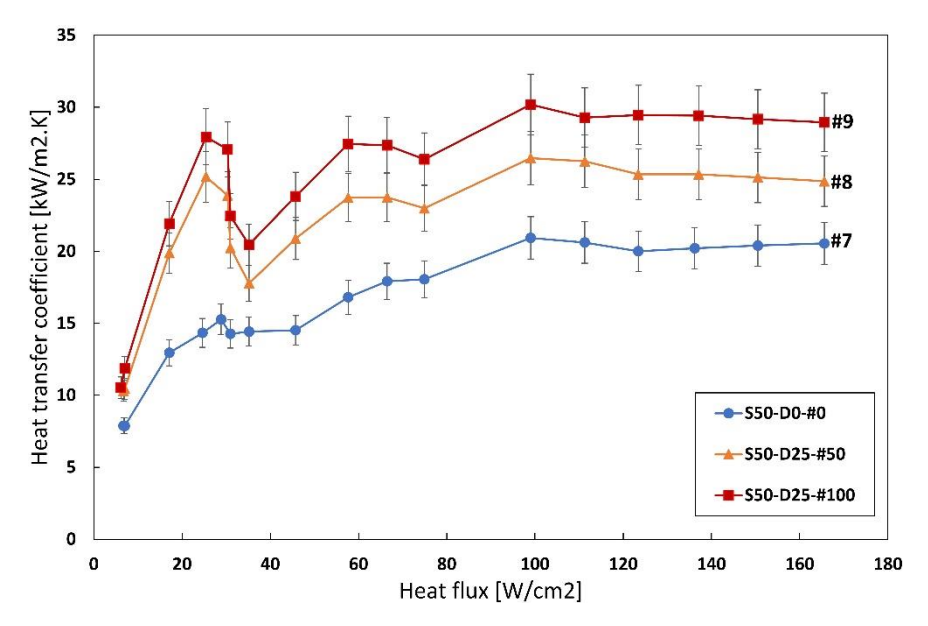


Figure 10. Comparison in heat transfer coefficient (HTC) for different surfaces with same spacing and different number of artificial cavities.

As shown in **Figure 10** HTC increases with the number of cavities. An increase in the number of artificial cavities leads to an increase in active nucleation sites, thereby enhancing boiling heat transfer.

2.2.2 The effect of microchannel spacing

Channel spacing is one of the important parameters affecting boiling heat transfer and behavior of the bubble on the departure time from the surface. In this section, the experiments were conducted at three different groups with different spacings and same cavity density. For a better understanding and detailed study, they were compared within three regions of heat fluxes: Low, Medium, and High heat flux (**Table 3**).

2.2.2.1 Samples without artificial cavities

The first group serves for revealing the effect of spacing for surfaces with microstructures without any artificial cavities. These surfaces correspond to samples #1,

#4, #7, and #10. First, at the low heat flux cases, the biggest spacing among these samples (#10) leads to a better performance compared to the other three samples and to smaller wall superheat temperatures. However, sample #1 with the smallest spacing performs better compared to samples with larger spacing (#4 and #7).

For the medium heat flux cases, with an increase in heat flux, the BHT performance of sample #1 improves and becomes even better than that of sample #10. The performances of samples #1 and #10 are still better than samples #4 and #7. For the high heat flux cases, the performance of sample #1 with the smallest spacing still remains better than the rest of the samples and is followed by sample #10 with the biggest spacing. In the meantime, it can be noticed that the performance of sample #7 slightly improves and becomes better than sample #4.

According to these observations, it can be concluded that the smallest spacing has a positive effect on the performance of the samples and is followed by the biggest spacing. However, the other two samples, which have rather a medium spacing, does not provide a high performance compared to the other ones. **Figure 11** shows the boiling images related to these four samples at different heat fluxes. It can be seen that, for the surface with the smallest S (sample #1), the number of nucleation points is more than the other surfaces, and with an increase in the heat flux, more nucleation points are activated, which continues until nucleation occurs on the entire surface. This finding is in agreement with the results in different studies [49,50,87], which reported that short spacing improves heat transfer. As the heat flux increases, the coalescing bubbles begin to form bubble groups and depart accordingly.

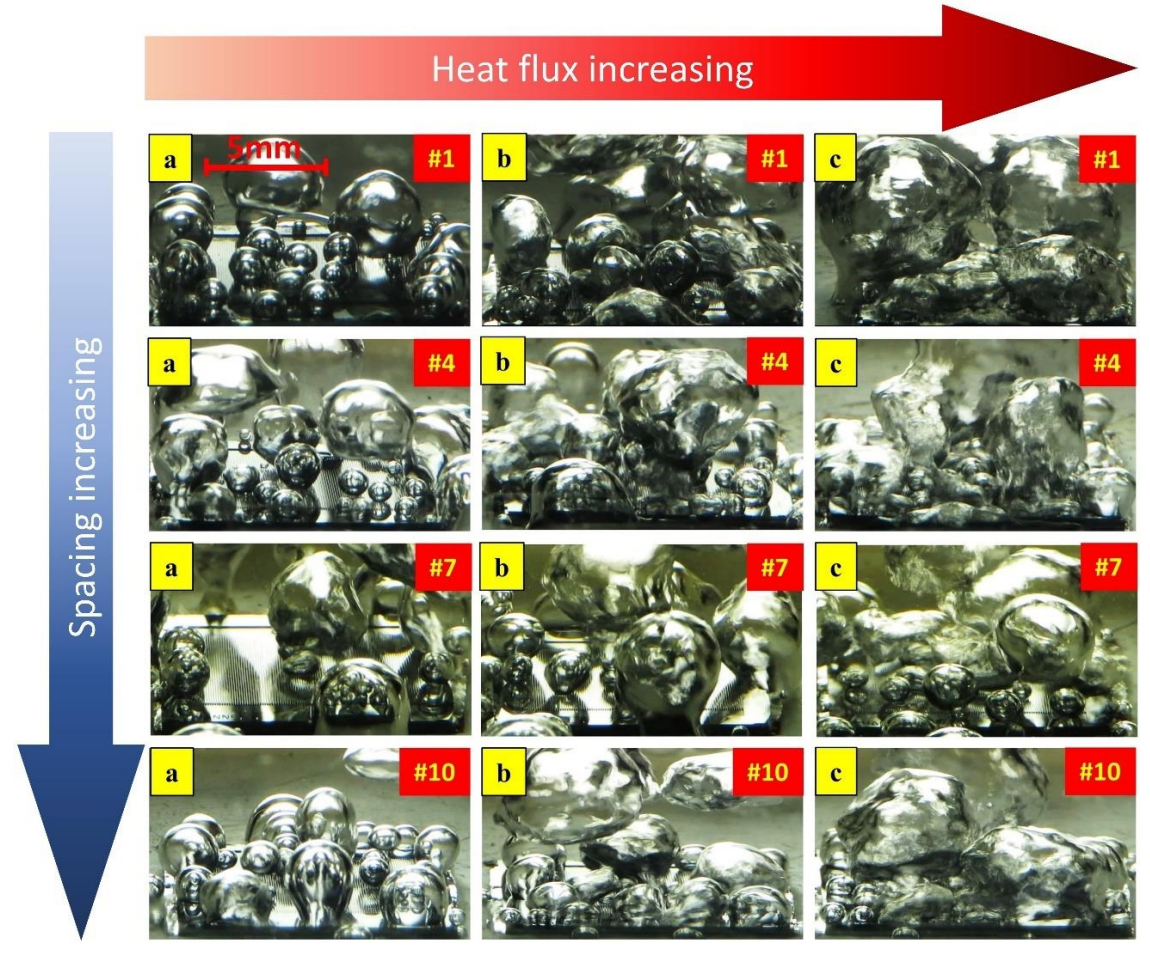


Figure 11. Different samples with different spacings and without artificial cavities. (a) heat flux $7.2(W/cm^2)$, (b) heat flux $45(W/cm^2)$, (c) heat flux $115(W/cm^2)$.

2.2.2.2 Samples with medium density of artificial cavities

In this section, samples with 50 artificial cavities are examined. The numbers of these samples by considering the spacing from smaller to bigger spacing are #2, #5, #8, and #11, respectively. As shown in **Figure 8**, when artificial cavities are added to the samples, at low heat fluxes, unlike in the case without any cavity, the performance of the sample with the largest spacing becomes lower than other surfaces with the same number of cavities. It can be seen that the performance of other surfaces with smaller spacings is close to each other, and only the performance of sample #5 is slightly better compared to samples #2 and #8. For the medium heat flux range, the performance of samples #2 and #11 improve such that sample #2 has the best performance in this range of heat flux compared to similar samples. For high heat flux values, sample #11 with the largest spacing, in the contrast to the low heat flux results, performs much better at high heat fluxes and has the best performance among those samples. In addition, the performances of all three samples #2, #5, and #11 are very close to each other, while sample #8, unlike other samples, has an inferior performance at high heat fluxes compared to other samples.

A possible reason for such a performance could be the mutual effect of nucleation site and spacing at this sample, in which the generated bubbles from microchannels coalescence with generated ones from artificial cavities and results in a sooner bubble departure from the substrate.

Considering the results obtained from the samples, which all contain 50 artificial cavities, it can be concluded that sample #11, which has the biggest spacing, gradually improves its performance with heat flux and has the best performance at high heat fluxes. **Figure 12** shows the visualization results related to these four samples at different heat fluxes. It is evident that, at low heat fluxes, artificial cavities cause the generation of some nucleation points on the whole surface. With an increase in the heat flux to 45 (W/cm²), as shown in **Figure 12b**, the number of nucleation sites also increases. On the surfaces with larger S, the size of the bubbles at departure is smaller, which is due to more space for feeding the surface with the fluid within the channel spacing areas. This was also reported in some studies [88,89] and confirms the subsequent increase in BHT.

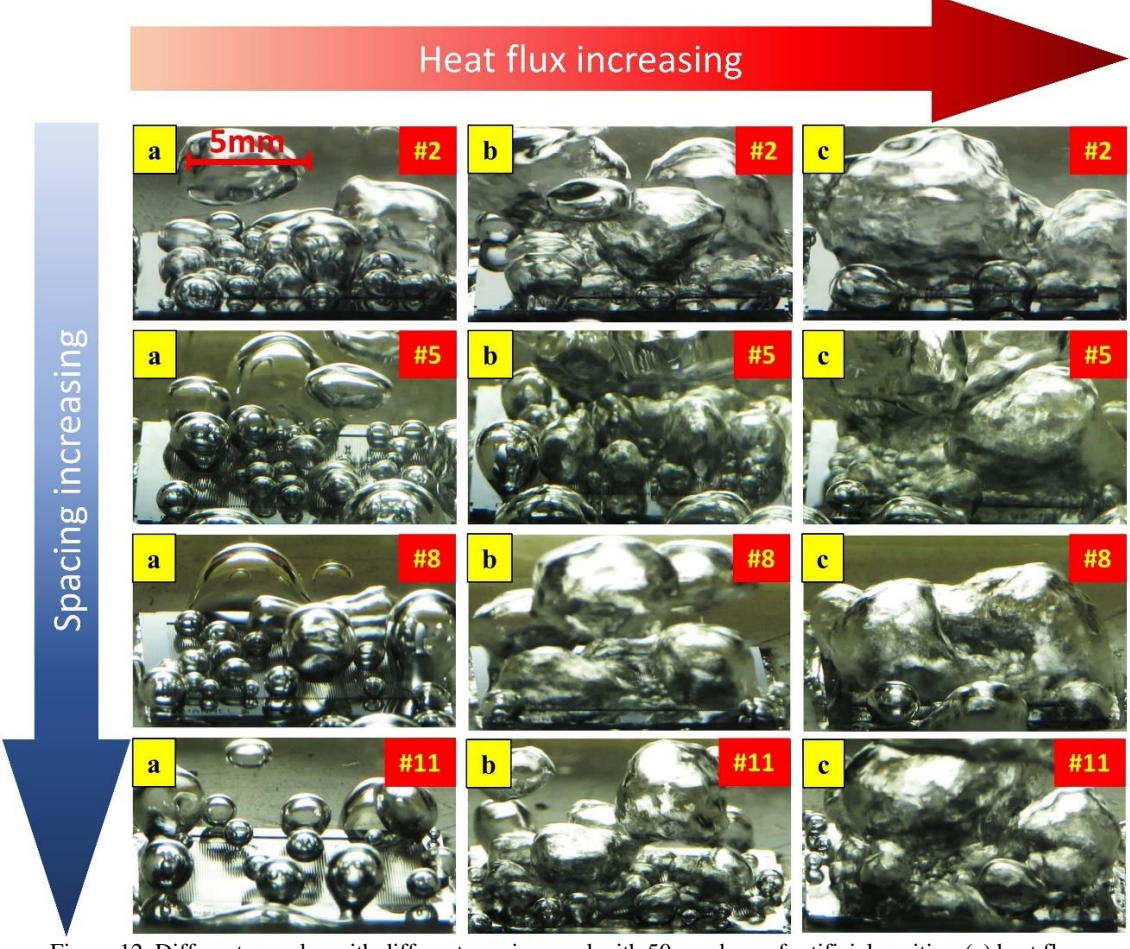


Figure 12. Different samples with different spacings and with 50 numbers of artificial cavities. (a) heat flux $7.2(W/cm^2)$, (b) heat flux $45(W/cm^2)$, (c) heat flux $115(W/cm^2)$.

2.2.2.3 Samples with high density of artificial cavities

The last category of samples performance comparison (shown in **Figure 8**) corresponds to the samples with the highest number of artificial cavities (100 artificial cavities on each sample) and includes samples #3, #6, #9, and #12 (from smallest to largest spacings). At low heat fluxes, samples #6 and #9 function almost identically and have the best performance among these four samples. Next to them are samples #3 and #12, respectively. At moderate heat fluxes, samples #6 and #9 maintain their relative superiority, whereas the performance of sample #12 becomes better than that of sample #3, and the performance of sample #3 also has a relative decline in the performance. For high heat fluxes, it is evident that the performance of sample #12 improves again and performs even better than samples #6 and #9, while sample #3 is relatively far from these other three samples.

Considering the BHT performance and behavior of the samples at different heat fluxes, it can be concluded that on the surfaces, where the most artificial cavities are located, the average spacing (neither the smallest nor the biggest) causes effective cooling at the low and medium heat fluxes, which implies an optimum configuration in terms of spacing. However, for the largest spacing, the surface BHT performance gradually improves with heat flux so that at it has the best performance among the samples high heat fluxes. This is why sample #3 with the smallest spacing does not perform well, and by increasing the heat flux, its difference in the performance from other samples increases. As reported in the study Jaikumar and Kandlikar [90], the optimum spacing is different depending on the operating conditions. Figure 13 shows the visualization results related to these four samples with artificial cavity number of 100 at three different heat fluxes (Low, Medium, and High heat flux). As can be seen in Figure 13b, at medium heat fluxes, the number of the small bubbles increases with the channel spacing, which results in a better performance for the surfaces with a larger spacing. With a further increase in the heat flux to 115 (W/cm²) (high heat flux zone), it is evident that bubbles become larger, and the coalescence can be widely recognized. With a decrease in the spacing, the bubbles grow to a larger size and can hardly detach from the surface, which assists in the formation of vapor blanket on the samples. Eventually, it can be concluded that the surface with the largest spacing (#11) has then a smaller bubble departure diameter, and the bubbles from this surface can detach faster than other surfaces, which enables rewetting and thus enhances BHT.

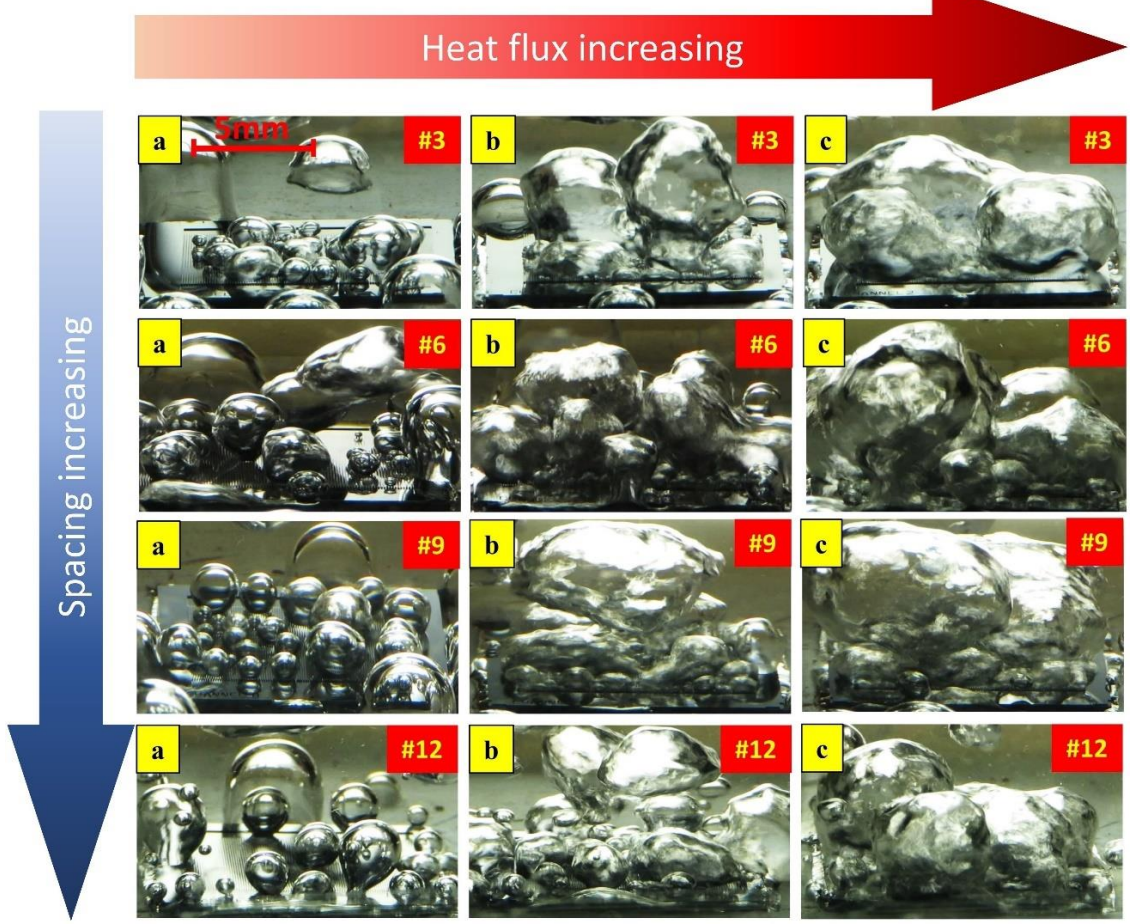


Figure 13. Different samples with different spacings and with 100 numbers of artificial cavities. (a) heat flux $7.2(W/cm^2)$, (b) heat flux $45(W/cm^2)$, (c) heat flux $115(W/cm^2)$.

Figure 14 displays HTC profiles of all tested samples and summarizes all the results, which are discussed above.

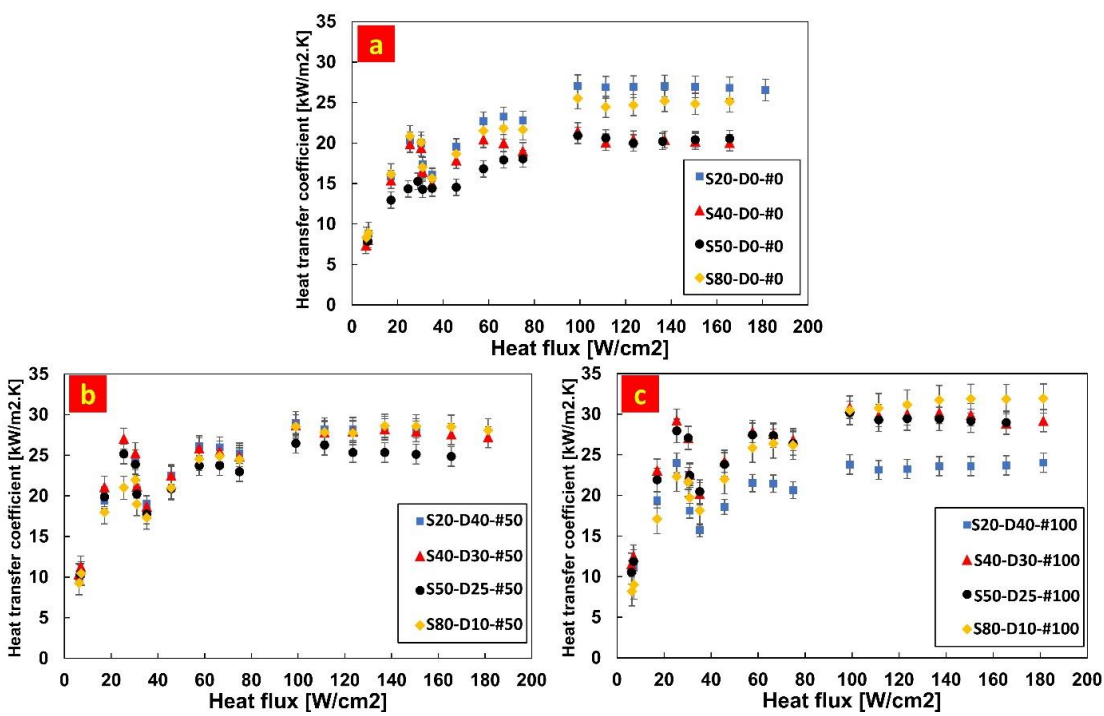


Figure 14. Heat transfer coefficient as a function of heat flux for a) samples without artificial cavities, b) samples with medium density of cavities c) samples with high density of cavities.

2.2.3 Critical heat flux (CHF)

In boiling heat transfer, critical heat flux (CHF) defines the operational limit and is recognized when a vapor layer begins to cover the heated surface, thereby considerably lowering heat transfer rate. In the literature, five possible pool boiling CHF mechanisms were reported [91]. A major mechanism is hydrodynamic instability presented by Zuber [92], which was the first physical explanation of the CHF phenomenon (**Figure 15**). Accordingly, CHF happens when the surface—fluid interface is broken due to the gravity-induced velocity differential between the rising vapor column and the falling liquid. For all the surfaces without artificial cavities, the probability of the vapor jets merging increases as the spacing increases. Therefore, vapor jets tend to coalesce at a lower altitude, which reduces CHF for samples with larger spacing. **Figure 16** shows the vapor blanket formation and departure for sample #10, which corresponds to the initiation of the CHF condition due to the hydrodynamic instability mechanism.

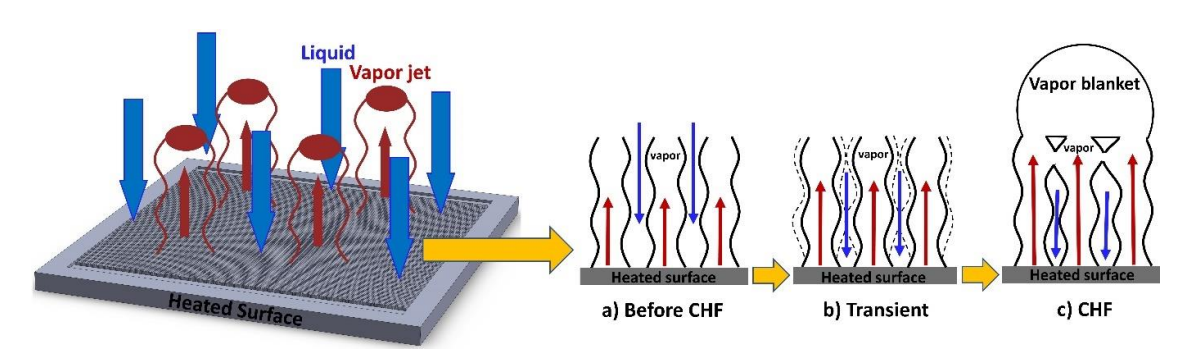


Figure 15. Schematic of the Zuber hydrodynamic instability model: (a) Vapor jet formation prior to CHF. (b) Vapor stem growth. (c) Vapor blanket formation due to Helmholtz instability. Adopted version from Liang and Mudawar [91].

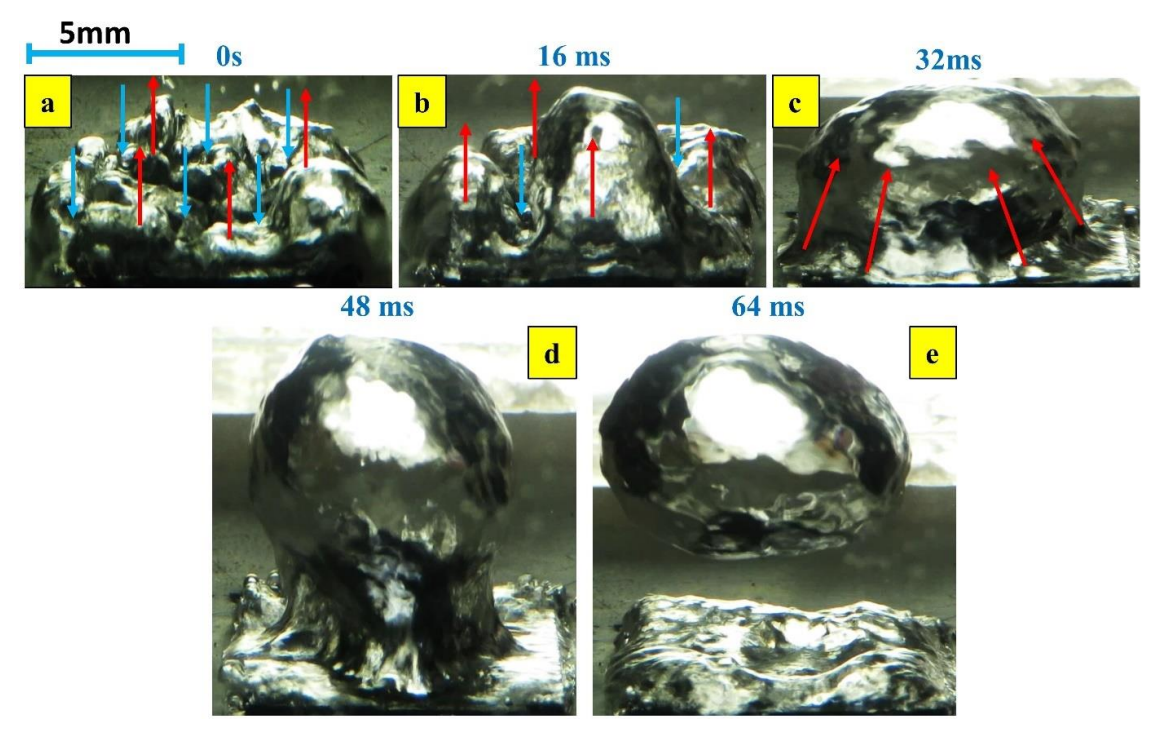


Figure 16. Vapor blanket formation due to hydrodynamic instability in surface #10 at CHF point (165.7 (W/cm²)).

The other important CHF mechanism is the microlayer dry-out [93] condition, where the vapor flow totally blocks the rewetting flow path at a CHF. On superheated surfaces, temporary dry-out is a result of this scenario. **Figure 17** shows the schematic of the Haramura and Katto's microlayer dry-out model [93]. On surfaces with artificial cavities, as discussed in the HTC results (**Figure 10**), the presence of artificial cavities raises the number of nucleation sites and improves boiling heat transfer. These nucleation points continue to generate bubbles at high heat fluxes with higher departure frequencies. This in turn leads to a presence of large number of bubbles on the surface and assists the formation of vapor blanket, which eventually causes the surface to reach CHF on the surfaces with artificial cavities. **Figure 18** shows the vapor blanket formation and departure for sample #3, which corresponds to the starting point of the CHF condition and dry-out. The red lines indicate small bubbles causing the formation of vapor blanket.

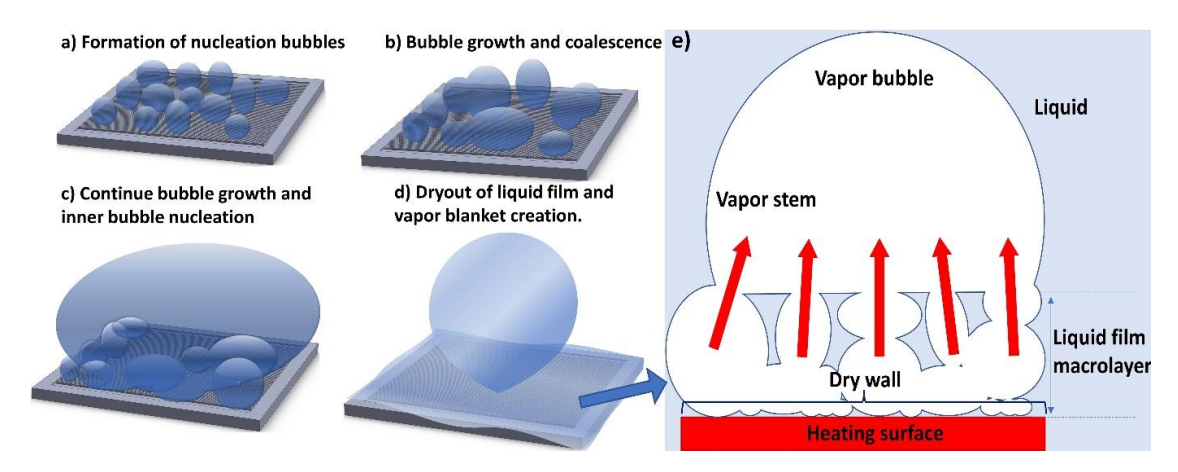


Figure 17. Schematic of Haramura and Katto's microlayer dry-out model.

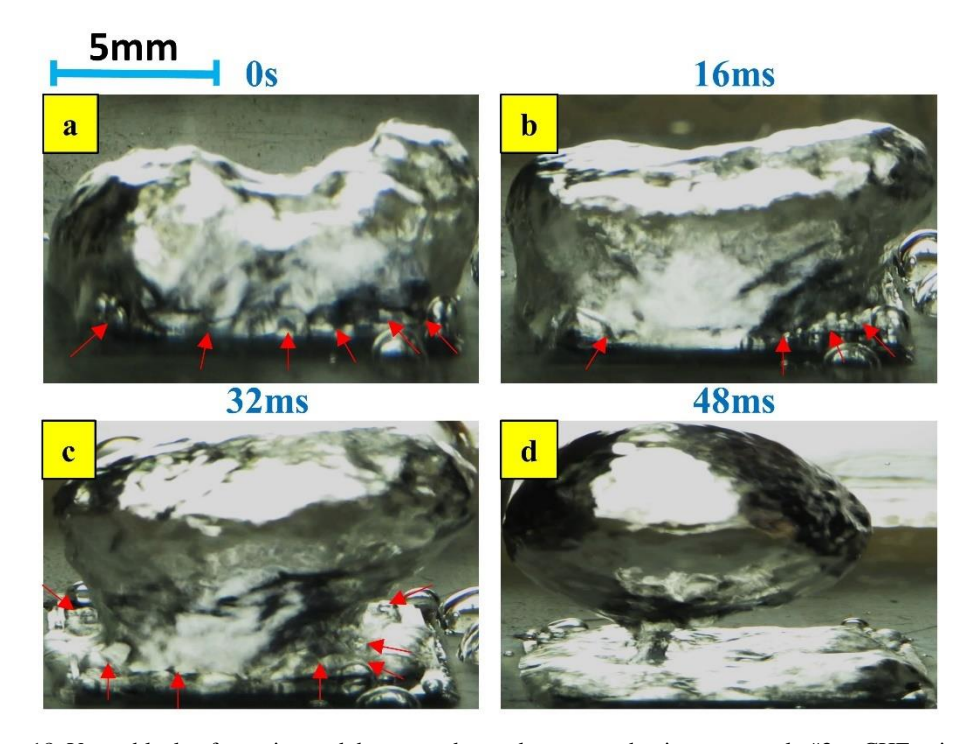


Figure 18. Vapor blanket formation and departure due to dry-out mechanism on sample #3 at CHF point (181 (W/cm^2)). (Red indicators show small bubbles)

Figure 19 displays CHF of the samples. As shown in **Figure 19**, it is evident that for most samples containing artificial cavities, CHF is extended. Samples #5, #6, #11, #12, and #3 can be considered as an example. But in the meantime, some samples act independently such as sample #2. For sample #2, it can also be observed that due to the artificial cavities size and small spacing on the microchannels, a vapor cloud forms on the surface more easily than the other samples.

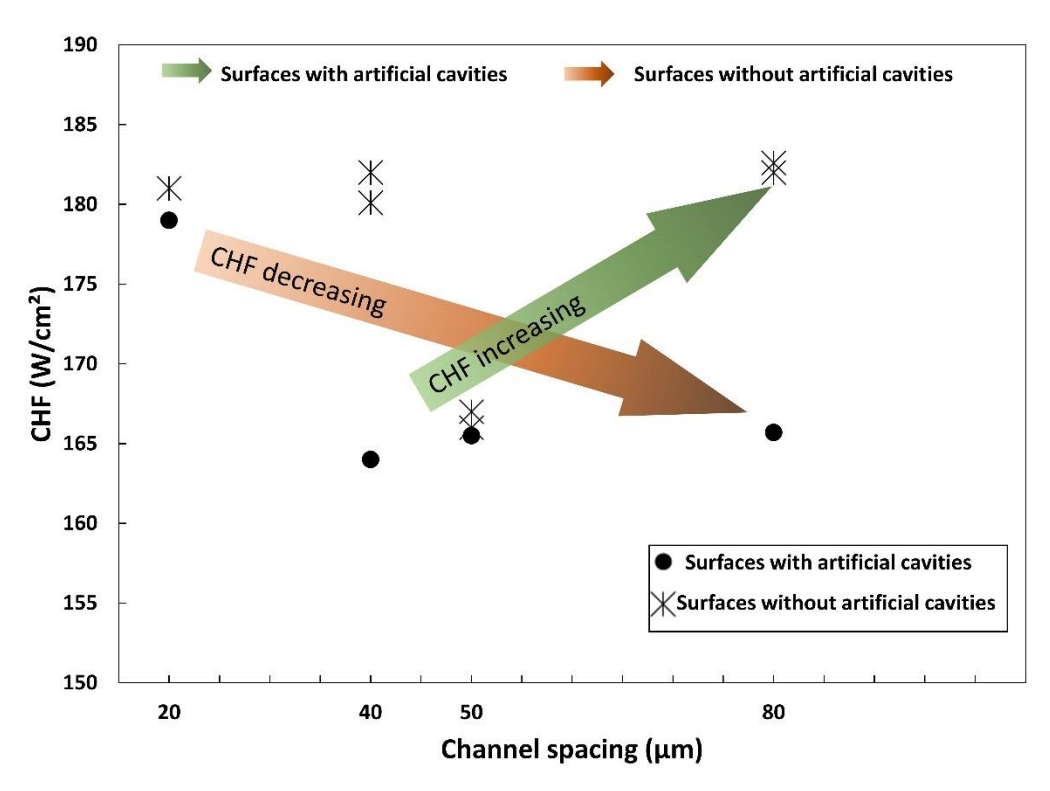


Figure 19. Effect of channel spacing and artificial cavities on the CHF for all the surfaces.

It is clear that with an increase in the number of cavities for different spacings, including S=40μm, 50μm, and 80μm, CHF can be enhanced. When comparing the same structures with different spacings, it can be concluded that for surfaces without artificial cavities, with an increase in channel spacing, CHF first decreases, and then there exists a plateau for increasing spacings. For the surfaces with an artificial cavity number of 100, CHF has the highest values, except surface #9, which has a lower CHF than the others. This result agrees with the reported data by Liang et al. [89] and Zhong et al. [29].

By considering visualization results, it is evident that for samples with artificial cavities, the microlayer dry-out mechanism is responsible from CHF, which is proven with the formation of a vapor blanket on the surface (**Figure 18**). This is valid for all surfaces except surfaces without artificial cavities. In this case, hydrodynamic instability triggers CHF (**Figure 16**).

Chapter 3. On saturated flow boiling heat transfer of deionized water and magnetic nanofluid on structured surfaces with and without external magnetic field

3.1 Bubble force analyses

A bubble grows until it reaches a certain size at the nucleation site and leaves the nucleation site. Then, it begins to slip forward on the surface. The bubble is lifted from the heating surface after moving along a certain distance. **Figure 20** depicts a schematic of the acting forces on a single bubble. The forces are extended in the X and Y directions for simplicity and are given as follows:

$$\sum F_x = F_{sx} + F_{sl} + F_{dux} + F_h + F_{cp}$$
 (3-1)

$$\sum F_{y} = F_{sy} + F_{duy} + F_{qs} + F_{b} \tag{3-2}$$

where F_s , F_{sl} , F_{du} , F_b , F_h , F_{cp} , F_{qs} are the surface tension force, shear lift force, unsteady drag force, buoyancy force, hydrodynamic force, contact pressure force, and quasi-steady drag force, respectively.

The forces in the y-direction try to lift the bubble from the heating surface, while the forces in the x-direction prevent attachment on the surface.

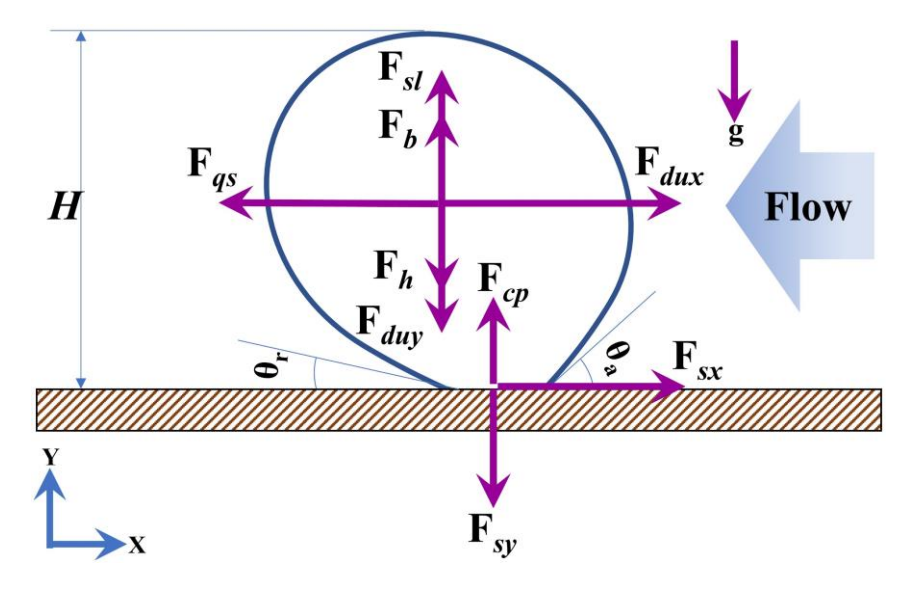


Figure 20. Force balance of a vapor bubble at a nucleation site.

3.1.1 Surface tension force

The surface tension forces in the x and y-axes are calculated follows [94]:

$$F_{sx} = -d_w \sigma \frac{\pi(\theta_a - \theta_r)}{\pi^2 - (\theta_a - \theta_r)^2} [\sin \theta_a + \sin \theta_r]$$
(3-3)

$$F_{sy} = -d_w \sigma \frac{\pi}{\theta_a - \theta_r} [\cos \theta_r - \cos \theta_a]$$
 (3-4)

In this equation θ_a , θ_r , d_w , and σ are the advancing contact angle, receding contact angle, bubble contact angle diameter, and surface tension, respectively.

3.1.2 Shear lift force

Over a wide range of Reynolds numbers, the shear lift force changes with the fluid velocity as follows [95]:

$$F_{sl} = \frac{1}{2}C_l u^2 \pi \rho_l r_b^2 \tag{3-5}$$

Here, u is the fluid velocity at the bubble center, and C_l is the shear lift coefficient, which is defined as:

$$C_1 = 3.877G_s^{\frac{1}{2}} (\text{Re}_h^{-2} + 0.014G_s^{2})^{\frac{1}{4}}$$
 (3-6)

where $G_s = \left| \frac{du}{dx} \right| \frac{r_b}{u}$, and $\text{Re}_b = \frac{2r_b u}{v_l}$ are the liquid shear gradient and bubble

Reynolds number, respectively.

3.1.3 Unsteady drag force

Due to the growth of bubbles, the unsteady drag force, also known as growth force, is represented as [96]:

$$F_{du} = -\rho_f \pi r_b^2 \left(\frac{11}{6}\dot{r}_b^2 + \frac{11}{2}r_b\ddot{r}_b\right)$$
 (3-7)

where \dot{r}_b and \ddot{r}_b are the first and second derivatives of the bubble radius with respect to time. The bubble radius (r_b) is expressed as [97]:

$$r_b = \frac{2b}{\sqrt{\pi}} Ja \sqrt{\alpha_f t} \tag{3-8}$$

where b is constant and taken 1.37 [95], and α_f is the thermal diffusivity. Ja is the Jacob number and is defined as:

$$Ja = \frac{\rho_f C_{pf} \Delta T_{sat}}{\rho_g i_{fg}}$$
 (3-9)

3.1.4 Buoyancy, contact pressure, hydrodynamic, and quasi-steady drag forces

All the above mentioned forces can be expressed using the following equations [94]:

$$F_b = \frac{1}{6}\pi d_b^{3} (\rho_l - \rho_g)g \tag{3-10}$$

$$F_h = \frac{9}{8}\rho_l U^2 \frac{\pi d_w^2}{4} \tag{3-11}$$

$$F_{cp} = \frac{\pi d_w^2 2\sigma}{4r} \tag{3-12}$$

$$F_{qs} = 6\pi v_l \rho_l U r_b \left(\frac{2}{3} + \left[\left(\frac{12}{\text{Re}_b}\right)^n + 0.796^n\right]^{-\frac{1}{n}}\right)$$
(3-13)

where d_b , ρ_l , ρ_g , σ , r, d_w are the bubble diameter, liquid phase density, vapor phase density, surface tension, bubble curvature radius, and bubble contact diameter, respectively. Also, in these equations, $U = u(r_b)$, n = 0.65, and $\text{Re}_b = \frac{2\rho_l U r_b}{\mu_l}$.

3.1.5 Presence of a magnetic field

An external magnetic field can be assumed to operate as a magnetic dipole [98] for actuation of magnetic nanoparticles. The applied magnetic force is defined as:

$$F_{m} = (m.\nabla)B \tag{3-14}$$

where m is the magnetic dipole moment, and B is the magnetic induction due to the external magnetic field. Rather than the magnetic field itself, the force acting on nanoparticles is dependent on the magnetic field gradient. The nanoparticle's magnetic moment, m, is a function of its magnetization:

$$m = MV_{np} (3-15)$$

where $M=\Delta\chi H$ is the volumetric magnetization of magnetic nanoparticles, and $\Delta\chi=\chi_{MNP}-\chi_{water}$, which is the effective susceptibility of the magnetic nanoparticles (by considering water as the medium), and $V_{np}=\frac{\pi D_{np}^3}{6}$, where D_{np} is the diameter of nanoparticles.

It is assumed that the nanoparticle's magnetization is saturated at all levels of an external magnetic field so that $\Delta\chi=\chi_{MNP}=\frac{M_{sp}}{H}$, where M_{sp} is the nanoparticle's saturation magnetization. The following expression can be derived by assuming that water's relative permeability $\mu_r=1$, together with $\mu_r=1$.

$$F_{m} = (m.\nabla)B = \frac{V_{np}M_{sp}}{R}(B.\nabla)B$$
 (3-16)

By considering $\nabla \times B = 0$, the magnetic force is obtained as:

$$F_{m} = \frac{V_{np}^{M} s_{p}}{2B} \nabla(B.B) = \frac{V_{np}^{M} s_{p}}{2B} \nabla B^{2}$$
 (3-17)

3.2 Experiments

3.2.1 Experimental setup and procedure

Most of the available studies in the literature investigated boiling of ferrofluids in cylindrical channels or rectangular channels with a small aspect ratio (0.4<AR<4). In this study, we designed a high aspect ratio rectangular mini channel (AR>10) to gain some advantages, including a two-piece test section (up and down) to study the effect of the orientation angle of the heating block and the effect of the gravity force as well, a rectangular channel for better visualization, very narrow channel to study different other parameters and forces (**Figure 21**).

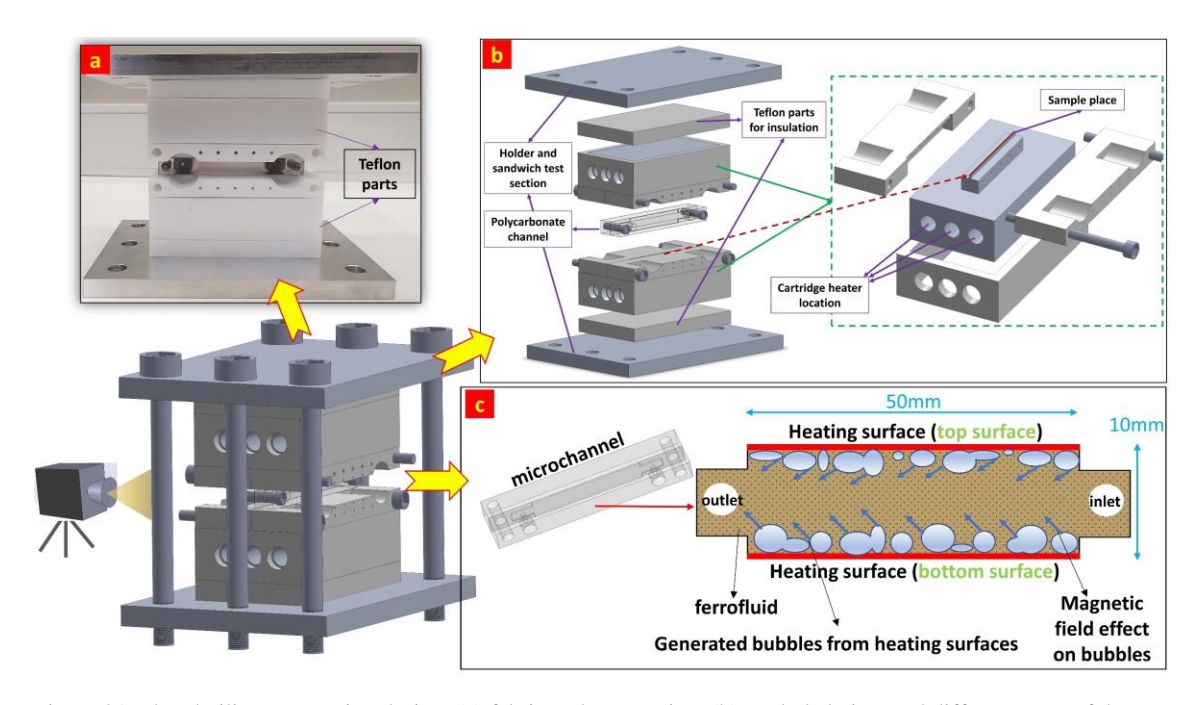


Figure 21. Flow boiling test section design: (a) fabricated test section, (b) exploded view and different parts of the test section, (c) microchannel schematic and place of the heating surfaces.

As can be seen in **Figure 21.b**, there are two aluminum blocks for heating with cartridge heaters and different Teflon parts for insulating the test section. Also, two different additional pieces of aluminum blocks were added to the bottom and top sides to package the test section and to hold all the parts at their prescribed locations. The most important part is the test channel made of polycarbonate, which is more durable than plexiglass to high temperatures and pressures. The size of the channel cross-section is $0.5 \, (\text{mm}) \times 10 \, (\text{mm})$, while its length is $50 \, (\text{mm})$. As shown in **Figure 21.c**, different bubbles are generated from heated surfaces on the top and bottom sides of the channel, while the applied magnetic field effect make them move and detach from the heated surface in a faster fashion.

As can be seen in **Figure 22**, the experimental setup, including a nitrogen tank for pumping the fluid, the fluid container at high pressure, a water bath, and some pressure sensors and thermocouples, for capturing pressure and temperature data, were used. First, the fluid container was filled with the working fluid from the top. Thereafter, a nitrogen tank pushed the nitrogen into the fluid container, and pressure was increased up to 4(bar), which was measured by a pressure sensor and enough for achieving the desired flow rate. We utilized a water bath as a preheater to heat the fluid to the saturation temperature. For this purpose, the water bath was heated up to 135°C to have the saturated condition before the test section inlet. For capturing boiling images, a high-speed camera and illumination source were used to visualize the flow inside the test section. The fluid passed through the test section and was guided into another fluid container after leaving the test section's outlet. A power supply was used to heat six cartridge heaters inside the aluminum blocks at the top and bottom sides of the channel. By increasing voltage, the heat flux was raised so that the experimental data could be acquired at different heat fluxes under steady state conditions.

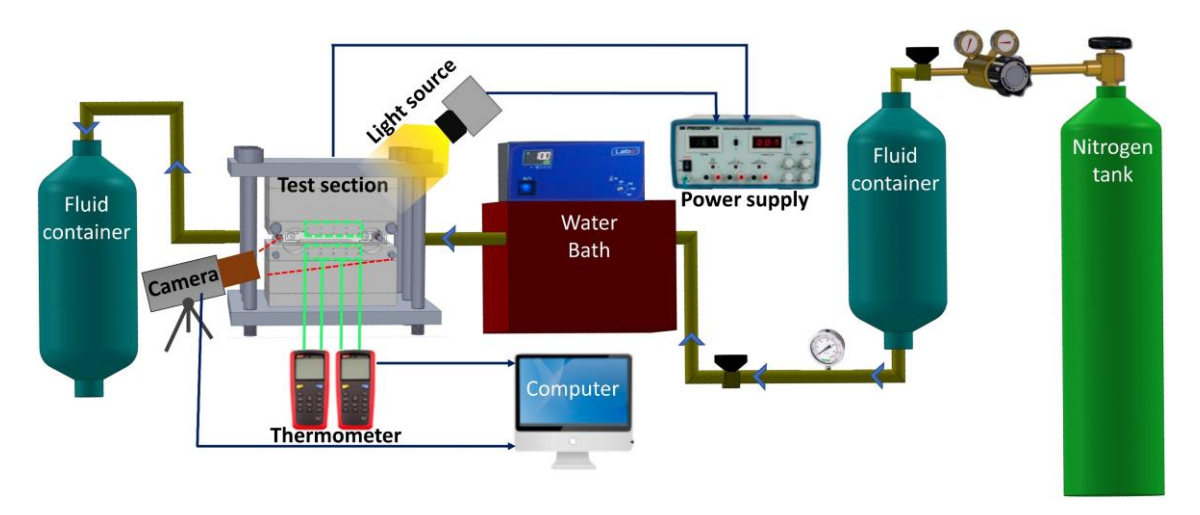


Figure 22. Schematic of the experimental setup for flow boiling tests.

First, the experiments were performed with DI water, and after finishing all the necessary tests, the tests focused on ferrofluid as the working fluid. In the final step, the external magnetic field was applied to the setup to reveal the effect of the external magnetic field in the setup (**Figure 23**). It should be noted that the external magnetic field magnetic flux density was 3.7 (mT) for experimental tests, which was the maximum magnetic flux density for Helmholtz coils. The maximum magnetic flux density amount has been selected according to the available sizes and models of Helmholtz coils and how

it is located around the test section by considering our limitations for visualization camera place.

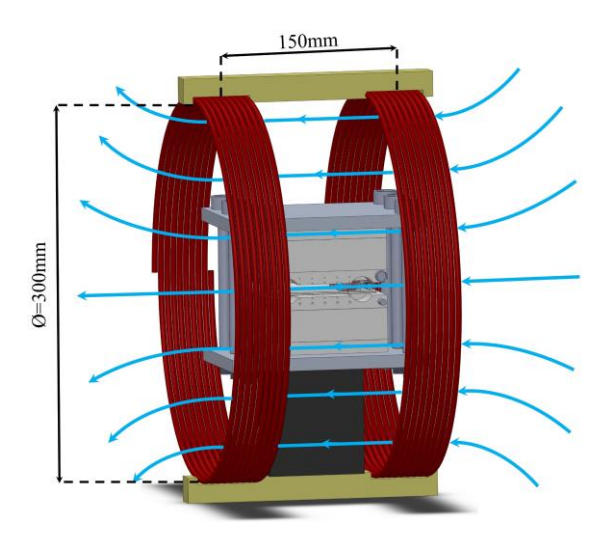


Figure 23. Using Helmholtz coils as an external magnetic field around the test section. The distance between two coils is 150mm, and the diameter of each coil is 300mm.

3.2.2 Ferrofluid and magnetic field characterization

3.2.2.1 Ferrofluid preparation

To prepare ferrofluids, we used two different types of nanoparticles. The first one is Lauric Acid (LA) coated Superparamagnetic Iron Oxide Nanoparticles (SPION), and the second one is Polyacrylic Acid (PAA) coated SPION (**Figure 24**).



Figure 24. Two different types of nanofluids.

The initial volumetric concentrations of these nanoparticles were 5%. DI water was added to the main fluids for the preparation of desired diluted ferrofluids to ensure stability. **Figure 25** shows the prepared stable fluids with a 0.02% volume fraction in parallel with the literature [99]. As shown in Fig. 8, the other prepared fluids with different volume fractions of PAA-coated nanoparticles including 0.6%, 0.4%, 0.2%, and 0.1% are not stable, and nanoparticles precipitated after a short time. Moreover, the

Figure 26, LA-coated nanofluid was not stable for a long time; therefore, to ensure that our ferrofluid is stable, we decided to continue with all the tests with PAA-coated nanoparticles.

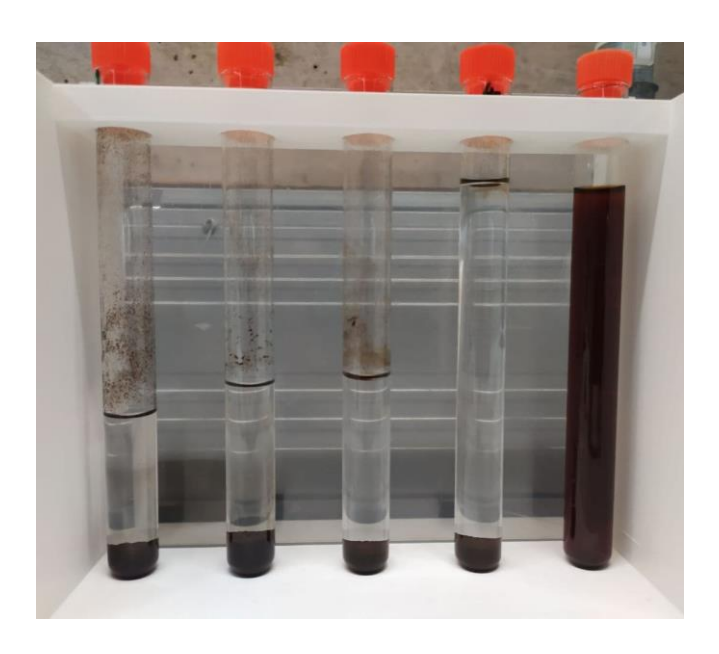


Figure 25. Different dilutions of nanofluids



Figure 26. Different dilutions (a) after mixing (b) after one day (c) after one week (1: LA 0.01%, 2: LA 0.02%, 3: PAA 0.02%)

3.2.2.2 Magnetic field characterization

To provide the necessary magnetic field for nanoparticle actuation and to allow visualization, we decided to use Helmholtz coils, which are a type of electromagnets as indicated in **Figure 27**. They could generate the desired magnetic field around the channel with a magnetic flux density of about 3.7 (mT).



Figure 27. Helmholtz coils produce an external magnetic field.

Two narrow pairs of coils with a radius R=150 (mm) were arranged in parallel with each other and on the same axis (with a distance (R)). The technical characteristics of the coil used in the experiments are shown in **Table 4**.

Table 4. Helmholtz coil characteristics

Description	Amount
Number of turns per coil	124 (turns)
Mean coil radius	150 (mm)
Coil spacing	150 (mm)
Maximum coil current	5 (A)
Maximum coil voltage	6 (V)
Maximum flux density at 5 (A)	3.7 (mT)

The magnetic field of each coil is non-uniform. When the distance between the two coils is equal to the coil radius, the magnetic field between the coils becomes uniform. The two field' superimposition of pair of coils produces a largely uniform magnetic field in the middle of (R) distance. The magnetic field strength changes with the distance as shown in **Figure 28** for each coil individually and an overall value for the pair of the coils.

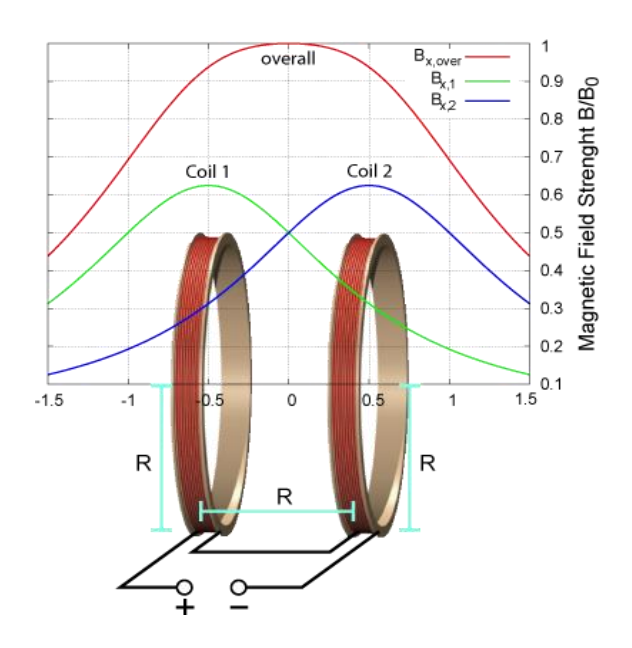


Figure 28. Magnetic field intensity of each coil and the overall value of the magnetic field at different locations [100].

For a single coil with a distance R/2 from the origin, the magnetic flux density is expressed as:

$$B(z) = \frac{\mu_0}{2} \cdot \frac{NIR^2}{\left[R^2 + (Z + \frac{R}{2})^2\right]^{(\frac{3}{2})}}$$
(3-18)

where N, R, μ_0 , *I, and Z* are the number of turns in each coil, mean coil radius, magnetic field constant, current in the wire, and distance of each coil from the center, respectively.

The magnetic flux density of the Helmholtz coils can be calculated using the Biot-Savart equation for the distance Z=R/2 from the origin using the following formula:

$$B(z) = 0.5 \mu_0 INR^2 \left\{ \left[R^2 + (Z + \frac{R}{2})^2 \right]^{\left(-\frac{3}{2}\right)} + \left[R^2 + (Z - \frac{R}{2})^2 \right]^{\left(-\frac{3}{2}\right)} \right\}$$
(3-19)

For the Helmholtz pair of coils, with the technical characteristics of the coil when z=0 and $\mu 0 = 4\pi \times 10^{-7} (\frac{H}{m})$ we can get: $B = 7.433 \times 10^{-4} I(T)$. Then, the magnetic field intensity at the center of each coil is: $B = 7.063 \times 10^{-4} I(T)$.

To validate the experimental results, preliminary experiments were performed with a gauss meter. The results of the measurements with a gauss meter were compared with the theoretical results for each coil separately and both coils together. In order to perform experiments, a (DC) power supply 5(A) at 230(V) and a gauss meter was used

based on the coil's instruction sheet. A single power supply was used to obtain a uniform current for both coils. The transverse probe of the gauss meter was used for the measurements. The Hall probe, which is the most important part of the gauss meter, is normally flat to make it suitable for measuring transverse magnetic fields. Axial probes were used to measure fields that were parallel to the probe. The gauss meter was adjusted on the (DCpk) mode, which means that the maximum positive peak reading of the DC electric field. The coils were connected in series to the DC power supply via connection cables. The power supply was set at 2.5 (A). **Table 5** shows the results of the measured and calculated magnetic field intensity.

 Coil 1
 Coil 2
 Both coils (measured)
 Both coils (calculated)

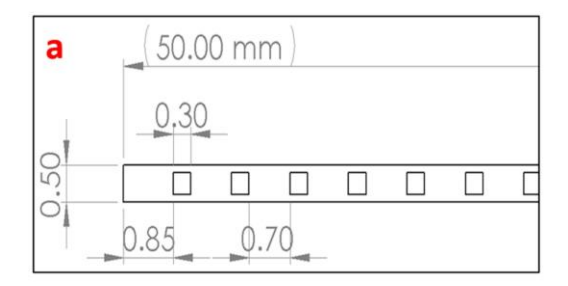
 1.822 (mT)
 1.864 (mT)
 1.850 (mT)
 1.858 (mT)

Table 5. Measured values of the magnetic field intensity and calculated values

The value of magnetic flux density from the measurements was 3.68 (mT) for a maximum current of 5(A). As a result, all the experiments with the magnetic field were performed at a 3.7 (mT) magnetic flux density.

3.2.3 Sample preparation and characterization

Two-side polished silicon wafers were used. First, the wafers were cleaned using acetone, IPA, and DI water and were then blown with nitrogen gas to ensure that they were free of contaminants. As can be seen in **Figure 29**, structured surfaces were designed to have different cavity patterns, including squares and circles with pitch sizes of 1(mm).



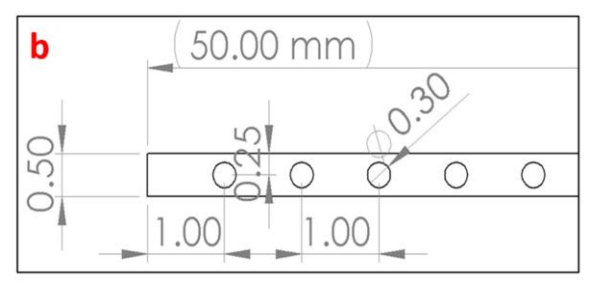


Figure 29. Structured surfaces with different cavity patterns, (a) square, (b)circular.

Cylindrical and square columns of cavities were formed on each surface (0.5mm \times 50mm) of two side polished silicon wafers with a 500 μ m thickness. The structures were

fabricated with the deep reactive-ion etching (DRIE) process capable. Since the DRIE was supposed to be used to etch the silicon thickness of 50μm, the resist would not have been survived to be used as a mask. Instead, an aluminum metal interlayer, which enjoyed a high selectivity compared to silicon under dry etching, was employed to serve as a mask. To this end, the E-Beam evaporation method was implemented to deposit a layer of 100 nm of aluminum (with a deposition rate of 1A/s and a vacuum of 5e-6 mTorr). Thereafter, in order to have the patterns on the Al film, a layer of photoresist (GXR-601) was spin-coated followed by soft backing, photolithography process, and development. Having the patterns inside the resist, they were transferred to the aluminum layer by wet etching. Subsequently, the PR was washed away with acetone, IPA, and DI water, and the sample was dried with nitrogen gas. The patterned aluminum layer was then employed as a mask for etching the underneath silicon by the DRIE process. **Figure 30** shows all steps of the fabrication process.

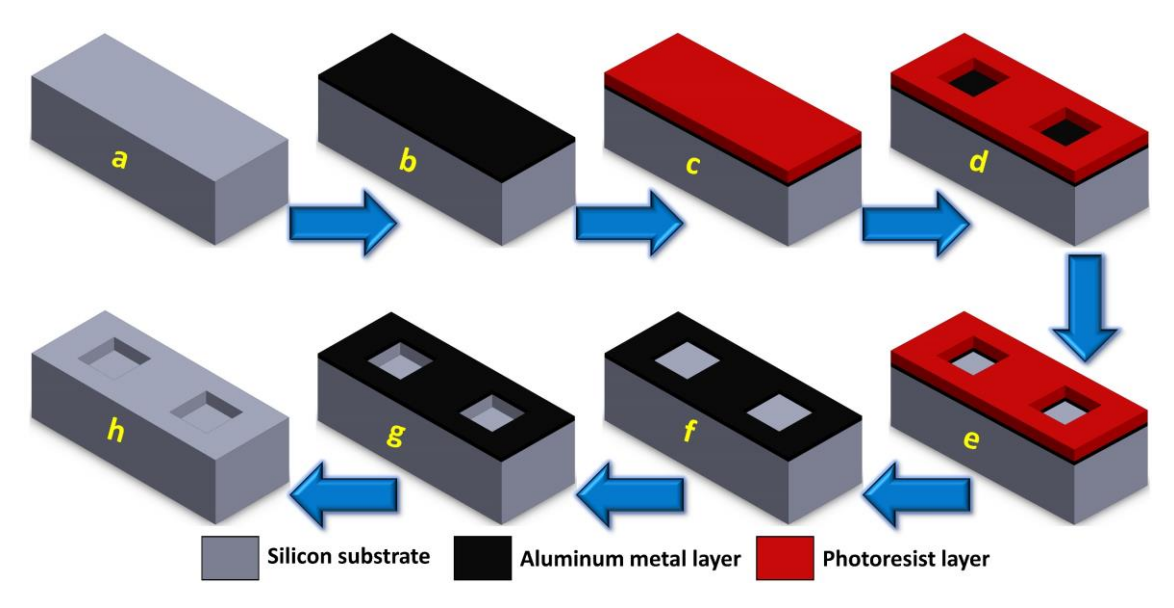


Figure 30. The fabrication process for structured surfaces. a)Silicon substrate, b)Al metal layer as a mask, c)Spin coated PR, d)Patterned PR by lithography, e)Patterned Al later by wet etching, f)PR washed away, g)Etching Silicon, h)Patterned surface after removing Al layer.

Figure 31 shows the mask design used during the fabrication process for different patterns with different pitch sizes and final diced samples to be used as substrate.

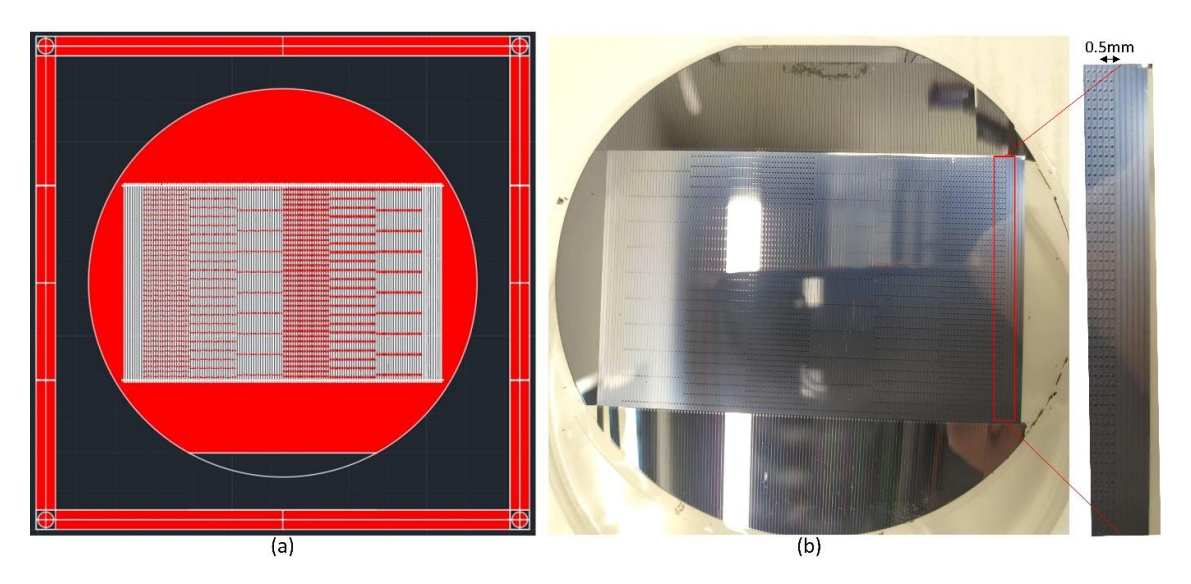


Figure 31. (a) Silicon wafer mask design for different pitch sizes, (b) Diced silicon wafer.

As can be seen in **Figure 32**, the contact angle of the channel wall, which was made of polycarbonate material, is about 90° . It is important to note that the contact angle of the polycarbonate walls, both the machined side and the bare side, were the same.

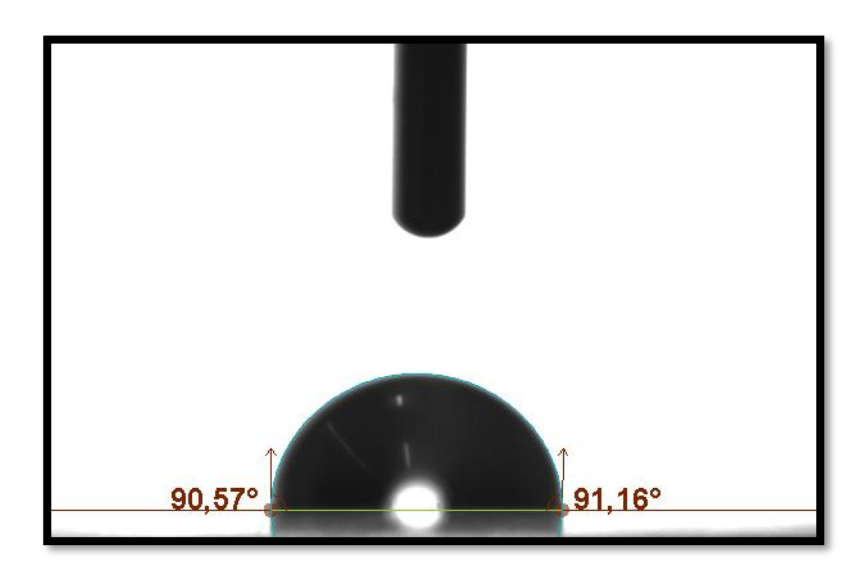


Figure 32. Contact angle of the channel wall made of polycarbonate

3.2.4 Data reduction and Uncertainties

The voltage, current, flow rate, and temperature data were used to calculate the mass flux and local and average heat transfer coefficients. The mass flux G was calculated as follows:

$$G = \frac{\dot{m}}{A_c} \tag{3-20}$$

where \dot{m} is the mass flow rate, and A_c is the cross-section area of the microchannel. Based on voltage and current values, the delivered electrical power can be calculated from the following formula:

$$P = V \times I \tag{3-21}$$

where V is the measured voltage, and I is the measured current. Furthermore, the heat flux can be expressed as:

$$\dot{Q} = \frac{(P - \dot{Q}_{loss})}{A_h} \tag{3-22}$$

where P is the applied net power to the system, \dot{Q}_{loss} is the heat loss, and A_h is the area of the heated surface. Heat losses (\dot{Q}_{loss}) were calculated using the surface heat loss estimation method for boiling tests. This required discharging the fluid from the system and starting to increasing power to the setup for heating. The temperature, as well as the applied power, were then recorded once the system reached the steady-state condition. As a result, a linear heat loss curve was plotted, which was then utilized to calculate heat losses.

Heat transfer coefficient (HTC) can be calculated from the following equation:

$$h = \frac{\dot{Q}}{(T_s - T_f)} \tag{3-23}$$

where T_f is the temperature of the working fluid (saturation temperature for saturated boiling), and T_s is the heated surface temperature, which is the average of five different $T_{s,i}$. As shown in **Figure 33**, by using the known applied heat flux and thermal resistances, the temperatures of the surface can be calculated as:

$$T_{s,i} = T_i - \dot{Q}(\frac{L_{Al}}{K_{Al}} + R_{TP} + \frac{L_{Si}}{K_{Si}})$$
 (3-24)

where $T_{s,i}$ is the surface temperature at each thermocouple position for (i=1 to 5), and T_i is the temperature recorded from the i^{th} thermocouple place. Furthermore, $L_{Al}, L_{Si}, K_{Al}, K_{Si}, R_{TP}$ represent the thickness of aluminum block, thickness of the silicon sample, thermal conductivity of aluminum, conductivity of silicon wafer, and thermal resistance of the thermal paste, respectively.

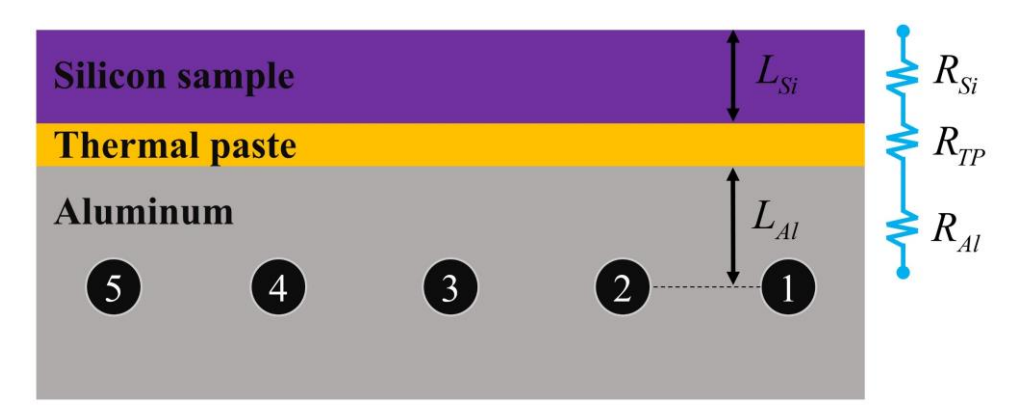


Figure 33. Schematic of thermocouple locations and approach (thermal resistance network) to calculate the surface temperature.

Table 6 summarizes the uncertainties in experimental parameter, which were based on the uncertainty propagation method (Coleman and Steck [84]).

Table 6. Uncertainties in experimental parameters.

Parameter	Uncertainty
Voltage [V]	±1
Current [A]	±0.1
Temperature [K]	±0.5
Dimensions [µm]	±15
Mass flow rate [kg/s]	±2-5%
Heat transfer coefficient [W/m ² K]	±4-6%

3.3 Results and discussion

3.3.1 Validation

Prior to conducting BHT studies, single-phase heat transfer tests were done to ensure that the experimental setup worked properly, and the obtained results were reliable. This validation was performed with DI water. Located thermocouples were utilized to acquire temperatures at the inlet and outflow of the test section to calculate the net power. As a result, the transferred heat to the fluid was obtained as follows:

$$\dot{Q} = \dot{m}c_n(T_{out} - T_{in}) \tag{3-25}$$

The average single-phase HTC was calculated as:

$$\bar{h} = \frac{\dot{Q}}{(T_{s,av} - T_{f,av})} \tag{3-26}$$

where $T_{s,av}$, $T_{f,av}$ are the average temperatures of the surface and fluid, respectively. The single-phase Nusselt number was calculated as:

$$Nu = \frac{\overline{h}D_H}{k_f} \tag{3-27}$$

where D_H is the hydraulic diameter of the channel, and k_f is the thermal conductivity of the working fluid. Moreover, the Reynolds number and Prandtl number are defined as:

$$Re = \frac{GD_H}{\mu}$$
 (3-28)

$$\Pr = \frac{c_p \mu}{k_f} \tag{3-29}$$

where G, μ are mass flux and dynamic viscosity of the fluid, respectively. Finally, the calculated single-phase average Nusselt numbers were compared with the Shah and London correlation [101], which is expressed as follows:

$$Nu = 1.953 (\text{Re.Pr.} \frac{D_H}{L})^{\frac{1}{3}} \text{ for } (\text{Re.Pr.} \frac{D_H}{L}) \ge 33.3$$
 (3-30)

$$Nu = 4.364 + 0.0722(\text{Re.Pr.}\frac{D_H}{L}) \text{ for } (\text{Re.Pr.}\frac{D_H}{L}) < 33.3$$
 (3-31)

For our operating conditions (Re.Pr. $\frac{D_H}{L}$) \geq 33.3, the first correlation (3-30) was used for the validation. **Figure 34** presents the comparison, and as can be seen, there is a close agreement between the experimental data and the predictions of the correlation (with a maximum mean absolute error of 7%).

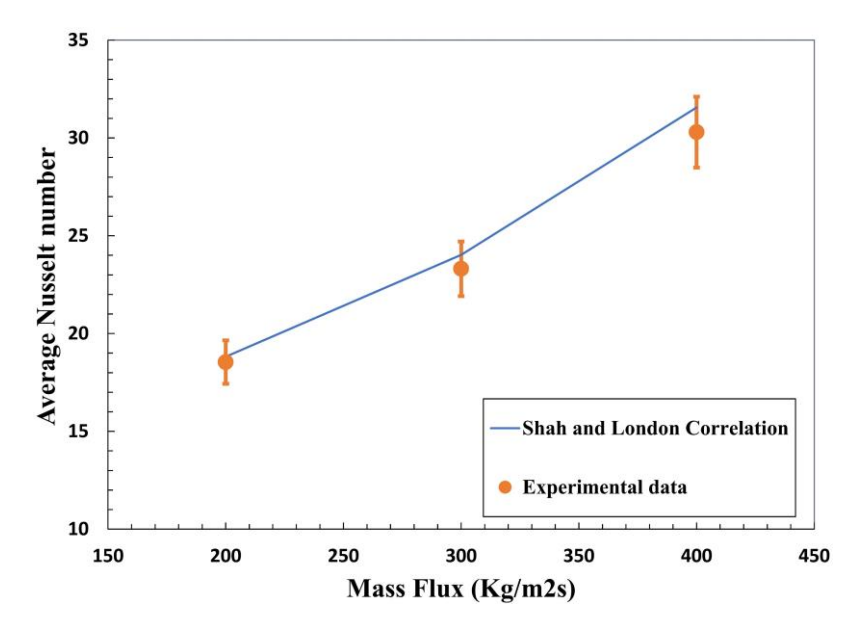


Figure 34. Validation of experimental results.

After validation tests with DI water, flow boiling heat transfer tests were done in the presence or absence of magnetic nanoparticles with and without an external magnetic field. The experiments were divided into three groups: DI Water (DW), ferrofluid without magnetic field (FF), and ferrofluid with a magnetic field (FF/MF). Moreover, there are two different heating blocks for the same heat fluxes, which are located on the bottom side (BS) and topside (TS) of the channel. All tests were performed at a mass flux of 300 (kg/m²s) within the heat flux range from 26.28 (W/cm²) to 142.8 (W/cm²).

3.3.2 Test with DI water (DW)

Figure 35 shows the visual results for DI water flow boiling experiments. On the bottom surface, the bubbles form from artificial cavities, grow with surface heat flux, and eventually depart. On the other hand, since the direction of buoyancy force is perpendicular and toward the top surface, the generated bubbles remain attached for a long time before rolling on the top surface, leading to the formation and existence of larger bubbles and slugs on the top surface compared to the bottom surface (Figure 35.c). Furthermore, the departed bubbles from the bottom surface contribute to slug formation near the top surface. As a result, much earlier CHF occurrence and surface temperature rise was observed on the top surface compared to the bottom one, as can be seen in Figure 35.d. Here, the CHF mechanism could be the sublayer dryout, where the liquid sublayer is completely dried while the large vapor blanket blocks the liquid wetting path. Boiling curves and HTC diagrams also confirm the visualization results. As shown in Figure 36, HTCs are higher for the bottom surface than the top surface.

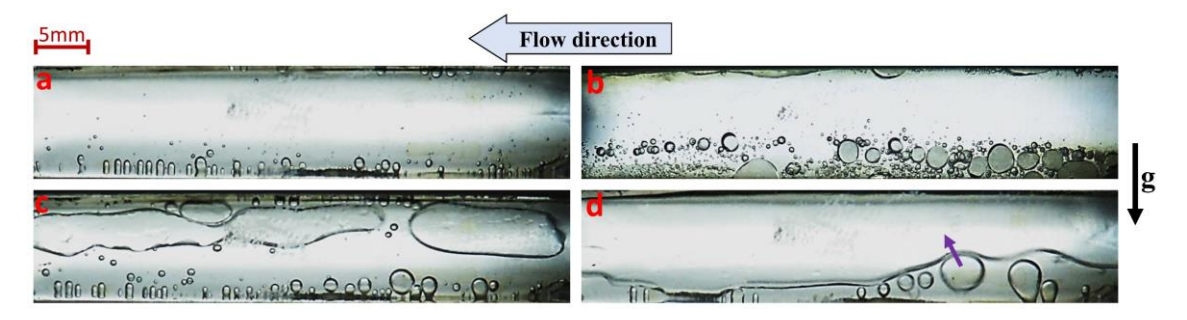


Figure 35. Boiling images at different heat fluxes and constant mass flux (G=300(Kg/m²s)). a) low heat flux, b) medium heat flux, c) high heat flux, d) dry-out for the topside heating surface, and bubbles which still generated from the bottom surface.

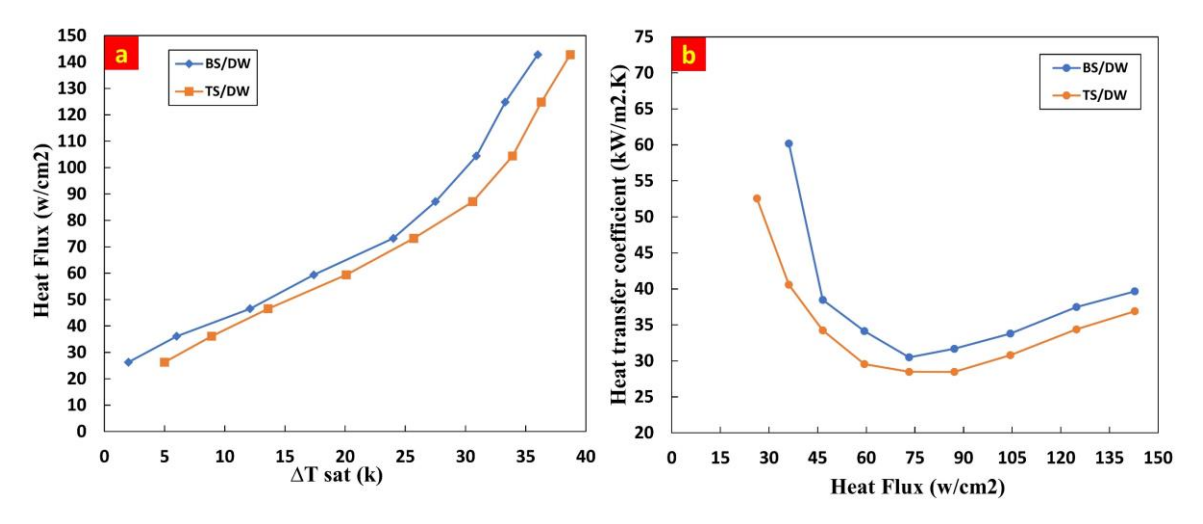


Figure 36. a) Boiling curves b) Heat transfer coefficients for the cases of heating blocks on top and bottom sides for ferrofluid.

3.3.3 Test with ferrofluid (FF)

The boiling curve and heat transfer coefficient results are shown in **Figure 38.a** and b for the ferrofluid flow boiling experiments. Similar to pure water, generated bubbles are larger on the top surface compared to the bottom surface. Here, the diameters of departed bubbles from the bottom surface are larger than for the deionized water flow boiling. An increase in surface wettability (due to nanoparticle deposition) could be a reason for a larger bubble departure diameter. On the top surface, while at medium heat fluxes a thin vapor layer was evident for the water case (**Figure 35.b**), smaller bubbles were observed in ferrofluid. A decrease in surface tension might be a reason for the formation of non-departed bubbles on the top surface (**Figure 37.b**). **Figure 38** depicts the heat transfer results for the top and bottom surfaces under the same wall heat flux conditions. **Figure 37** depicts that similar to pure water, the heat transfer performance of the bottom surface is superior, which is also a confirmation of visualization results. The dry-out condition occurs earlier on the top surface at high heat fluxes due to the gravity-induced bubble coalescence and large vapor blanket formation near the surface.

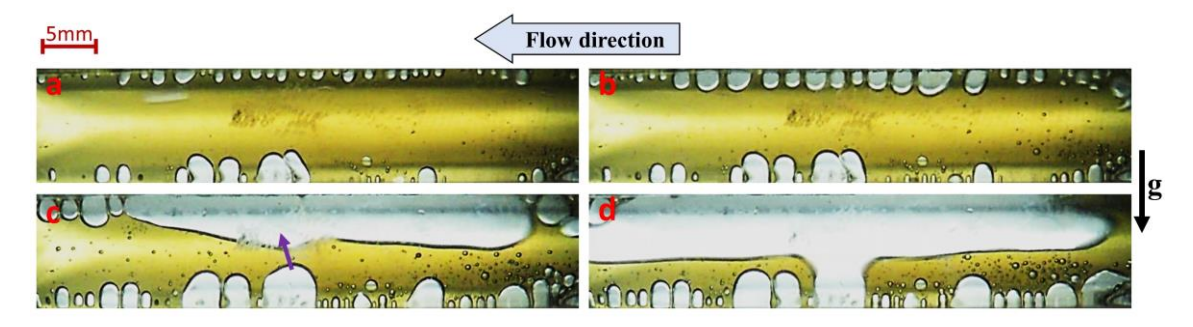


Figure 37. Ferrofluid boiling images without external magnetic field at different heat fluxes and constant mass flux (G=300(kg/m²s)). a) low heat flux, b) medium heat flux, c) high heat flux, d) dry-out for the top surface

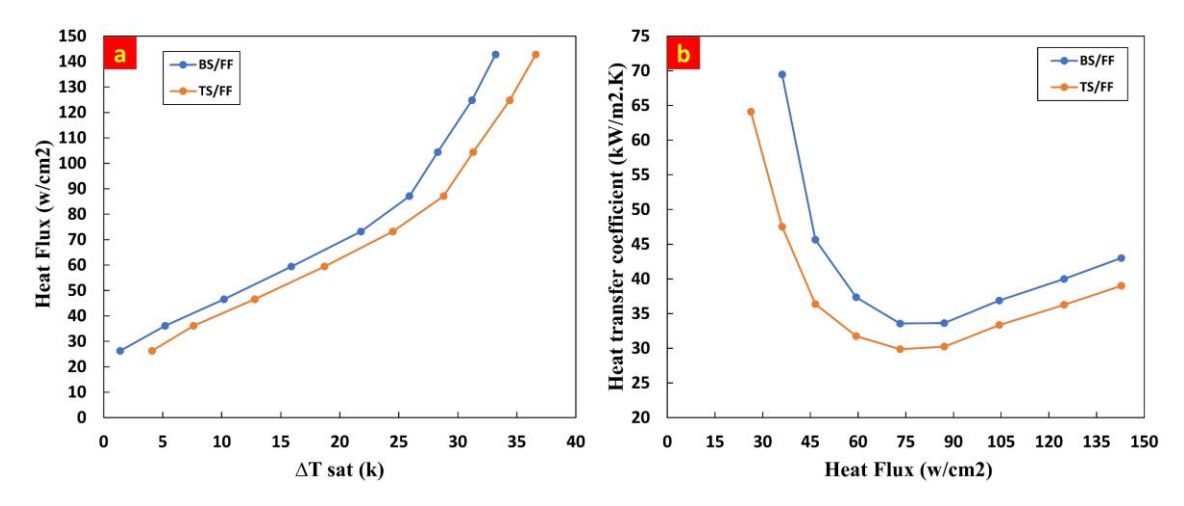


Figure 38. a) Boiling curves b) Heat transfer coefficients for the cases of heating block on top and bottom sides for ferrofluid without external magnetic field effect.

3.3.4 Test with ferrofluid and magnetic field (FF/MF)

For the last series of tests, an external magnetic field was applied to reveal the effect of the field. Due to the presence of a magnetic field, as shown in **Figure 39**, the bubble lift-off diameter decreases in the presence of the magnetic field. **Figure 40** shows the boiling curve and HTC for the top and bottom surfaces, and as expected, the heat transfer performance is better for the bottom surface similar to the previous cases. While there are small bubbles due to magnetic field, the magnetic field also make the bubbles detach from both top and bottom surfaces faster.

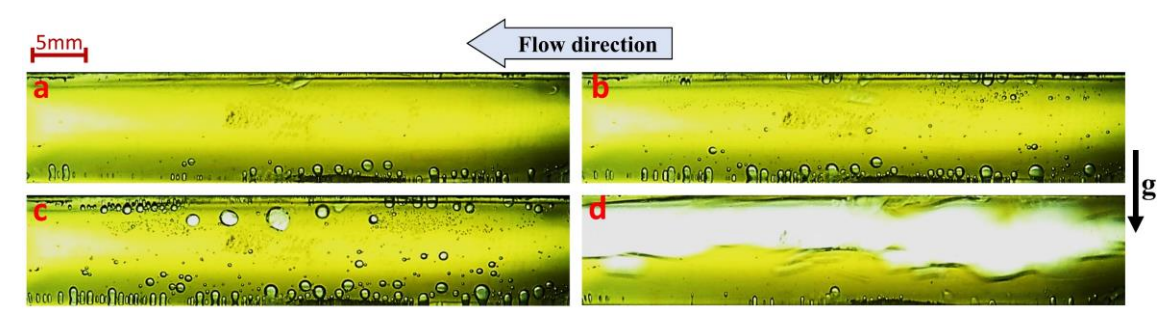


Figure 39. Ferrofluid boiling images in the presence of an external magnetic field effect (3.7 (mT)) at different heat fluxes and constant mass flux ($G=300(kg/m^2s)$). a) low heat flux, b) medium heat flux, c) high heat flux, d) dry-out on the top surface.

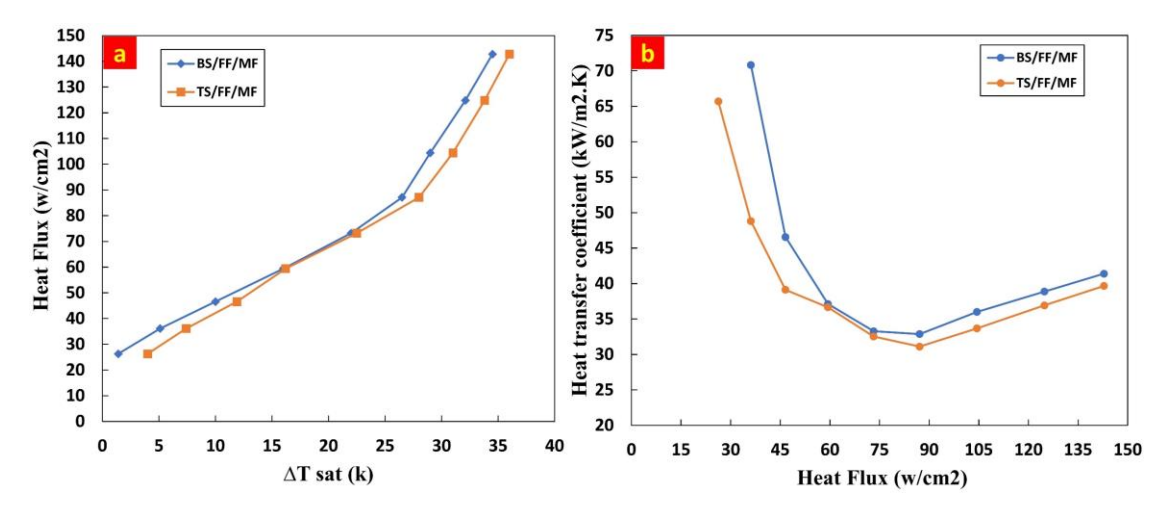


Figure 40. a) Boiling curves b) heat transfer coefficients of top and bottom surfaces for the ferrofluid case in the presence of external magnetic field.

3.3.5 Heat transfer results

As shown in **Figure 41 and Figure 42**, the heat transfer performance of flow boiling in a narrow microchannel enhances whit magnetic nanoparticles. The maximum HTC enhancement was 21.5% for FF in comparison with DW. Furthermore, comparing ferrofluid data in the presence and absence of a magnetic field, it was fund that for the bottom surface, where the surface is in the horizontal position, there is no significant change at low and medium heat fluxes. However, at high heat fluxes, the external magnetic field makes the bubbles stay on the heating surface for a longer period. As a result, heat transfer deteriorates when compared with the ferrofluid case in the absence of magnetic field (FF). On the other hand, for the top surface, application of magnetic field to ferrofluid causes faster detachment of bubbles so that heat transfer enhancement can be achieved with magnetic field (FF/MF). Finally, it can be stated that HTC enhanced up to 25% for the (FF/MF) case compared with (DW).

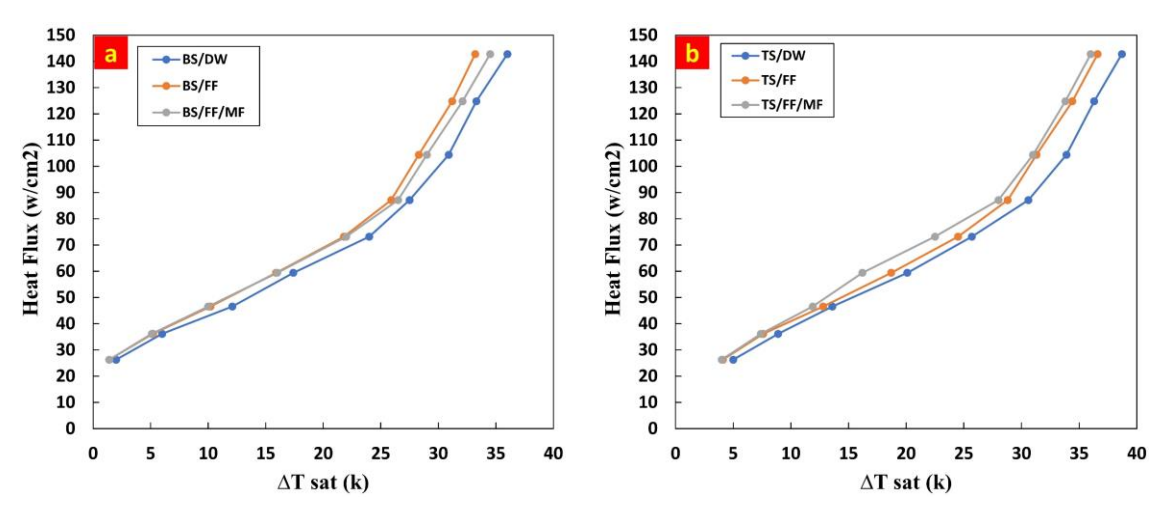


Figure 41. Boiling curves for different conditions a) bottom surface, b) top surface (G=300 (Kg/m²s)).

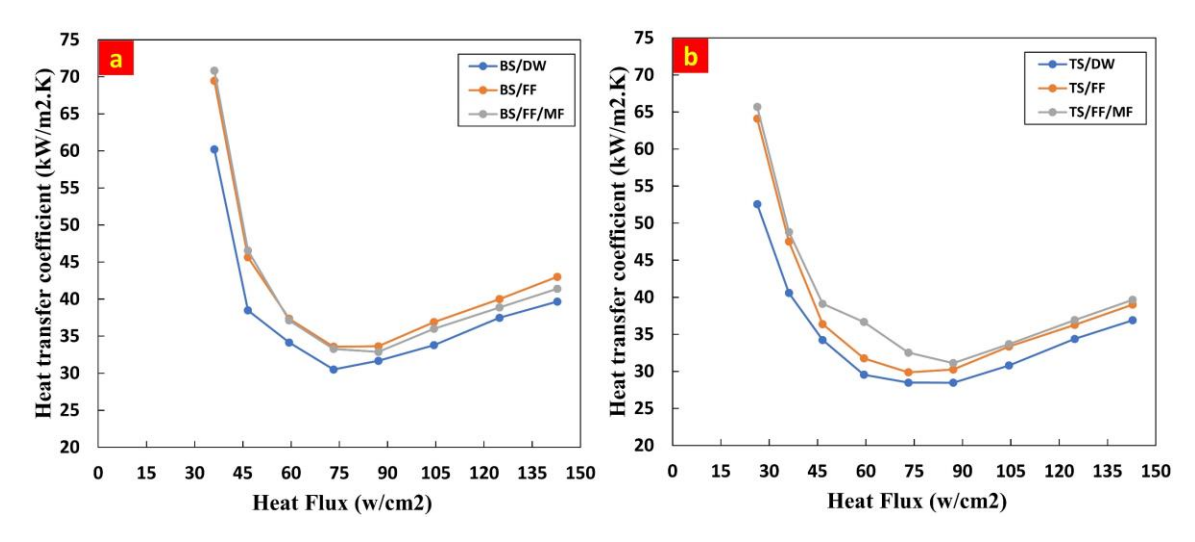


Figure 42. Heat transfer coefficients profiles for a) bottom surface and b) top surface.

The Scanning Electron Microscopy (SEM) technique was used to characterize the surface condition before and after ferrofluid experiments in the presence and absence of an external magnetic field. The SEM images are shown in **Figure 43**. Accordingly, nanoparticles fill the cavities on the surfaces and accumulate there. However, with an external magnetic field, nanoparticle accumulation on cavities is prevented.

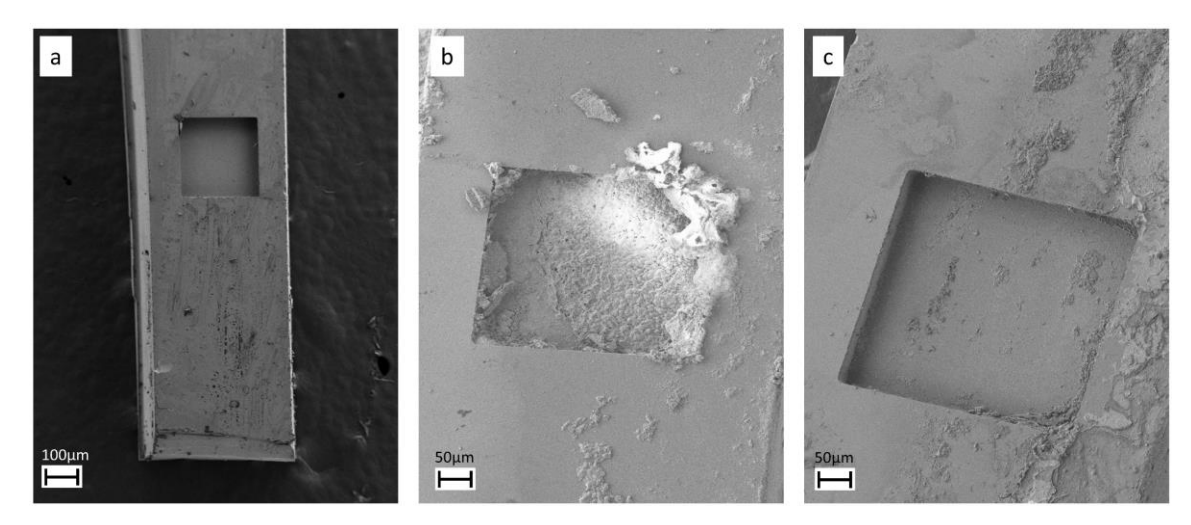


Figure 43. SEM images of silicon surface with square cavities a) before the test, b) tested with ferrofluid) tested with ferrofluid and external magnetic field effect.

Chapter 4. Conclusion and Future Works

4.1 Conclusion- A parametric study on pool boiling heat transfer and critical heat flux on structured surfaces with artificial cavities

A parametric study was conducted in this study to evaluate the effect of microchannel spacing and artificial cavities on BHT and CHF for 12 different structured surfaces with different configurations. Furthermore, by comparing the boiling curves for different samples, also with the help of visualization studies, the enhancement mechanisms of structured silicon surfaces are explained, and the following major conclusions are drawn:

- 1. By comparing samples with and without artificial cavities, it can be concluded that the BHT performance of different samples significantly improves for samples containing artificial cavities. As the number of cavities on the samples increases, the number of active nucleation points also increases, which ultimately improves the surface performance at different heat fluxes, especially at high heat fluxes.
- 2. For $S=20~\mu m$, the influence of microchannel spacing is more dominant than the number of cavities. While the microchannel configurations have no significant effect at low heat fluxes, increasing the heat flux reveals the surface structure effect on BHT and bubble dynamics.
- 3. For samples without artificial cavities, it can be concluded that the smallest spacing leads to the best BHT performance at high heat fluxes. This is because the vapor jets coalescence at a closer distance from the surface when the sample spacing increases, thereby making the rewetting process more difficult.
- 4. For samples with numbers of artificial cavities of 50 and 100, the biggest spacing leads to the best BHT performance at high heat fluxes. This is due to the combined impact of increased spacing and number of artificial cavities, which increase the number of nucleation sites.

5. The CHF on the structured surfaces with artificial cavities increases with the number of the cavities. Moreover, the results reveal that dry-out is the dominating CHF mechanism for surfaces with artificial cavities due to the creation of small bubbles on the surface from artificial cavities as nucleation sites, while hydrodynamic instability is the dominant CHF mechanism for surfaces without artificial cavities.

4.2 Conclusion- On saturated flow boiling heat transfer of deionized water and magnetic nanofluid on structured surfaces with and without external magnetic field

Flow boiling heat transfer in a minichannel having surfaces with square cavities was investigated for three different cases: pure DI water (DW), ferrofluid in the absence of an external magnetic field (FF), and ferrofluid in the presence of an external magnetic field (FF/MF). All the tests were done for a rectangular minichannel with two different heating blocks on the top and bottom sides of the microchannel with the use of a high-speed camera. The heat flux range was between 26.28 (W/cm²) and 142.8 (W/cm²), and the mass flux was 300 (kg/m²s), and tests were performed at the saturation temperature of the fluid, and the magnetic flux density was 3.7 (mT). The findings of this study are summarized as:

- Orientation of the heating surface has different effects on BHT due to the bubble departure frequency. For all the cases (DW, FF, and FF/MF), the heat transfer performance on the bottom surface is better than the top surface due to the larger bubble departure frequency on the bottom surface.
- 2. Upon addition of magnetic nanoparticles into DI water, nanoparticles lead to a larger bubble departure diameter for the (FF) case in comparison with the cases of (DW) and (FF/MF). The maximum HTC enhancement for (FF) in comparison with (DW) case was 21.5%.
- 3. Application of an external magnetic field to ferrofluid decreases the bubble departure diameter in comparison with the case of (FF). Furthermore, HTC enhanced in (FF/MF) case up to 25% compared with (DW).
- 4. At high heat fluxes, HTC on the bottom surface for the case (FF) is larger than the case (FF/MF) due to the dominant effect of the bubble coalescence at (FF), which is more than (FF/MF) condition and help to increase bubble departure frequency near the nucleation sites. On the other hand, HTC on the top surface for the case (FF/MF) becomes slightly better than the case (FF). The orientation of

the surface might make the merged bubble stay more for longer time on the surface, while bubbles could leave the surface faster with the help of an external magnetic field on magnetic nanoparticles.

5. An external magnetic field to ferrofluid results in less deposition of the magnetic nanoparticles on surface cavities, which act as nucleation sites on the surface. Thus, the magnetic field helps to maintain boiling heat transfer enhancement from the nucleation sites.

4.3 Future Works

Structural surfaces can play an essential role in boiling heat transfer. They can be employed in various applications with different uses of passive and active methods. The following research directions are recommended for the future:

- Effect of the acoustic field on pool boiling heat transfer with various structured surfaces.
- Using different patterns and materials to fabricate different kinds of structured surfaces.
- Using different working fluids such as refrigerants with magnetic nanoparticles in the presence of a magnetic field to investigate BHT in different pool and flow boiling setups.
- Study a single bubble behavior in flow boiling and pool boiling with different working fluids and magnetic nanoparticles in the presence of an external magnetic field.

BIBLIOGRAPHY

- [1] J. Kim, J.S. Lee, Numerical study on the effects of inertia and wettability on subcooled flow boiling in microchannels, Appl. Therm. Eng. 152 (2019) 175–183.
- [2] S. Ujereh, T. Fisher, I. Mudawar, Effects of carbon nanotube arrays on nucleate pool boiling, Int. J. Heat Mass Transf. 50 (2007) 4023–4038.
- [3] D. Cooke, S.G. Kandlikar, Effect of open microchannel geometry on pool boiling enhancement, Int. J. Heat Mass Transf. 55 (2012) 1004–1013.
- [4] M. Karimzadehkhouei, M. Shojaeian, K. Şendur, M.P. Mengüç, A. Koşar, The effect of nanoparticle type and nanoparticle mass fraction on heat transfer enhancement in pool boiling, Int. J. Heat Mass Transf. 109 (2017) 157–166.
- [5] M. Shojaeian, A. Koşar, Pool boiling and flow boiling on micro- and nanostructured surfaces, Exp. Therm. Fluid Sci. 63 (2015) 45–73. https://doi.org/10.1016/j.expthermflusci.2014.12.016.
- [6] A.K. Sadaghiani, R. Altay, H. Noh, H.J. Kwak, K. Şendur, B. Mısırlıoğlu, H.S. Park, A. Koşar, Effects of bubble coalescence on pool boiling heat transfer and critical heat flux A parametric study based on artificial cavity geometry and surface wettability, Int. J. Heat Mass Transf. 147 (2020) 1–15. https://doi.org/10.1016/j.ijheatmasstransfer.2019.118952.
- [7] A.R. Motezakker, A.K. Sadaghiani, S. Çelik, T. Larsen, L.G. Villanueva, A. Koşar, Optimum ratio of hydrophobic to hydrophilic areas of biphilic surfaces in thermal fluid systems involving boiling, Int. J. Heat Mass Transf. 135 (2019) 164–174. https://doi.org/10.1016/j.ijheatmasstransfer.2019.01.139.
- [8] V.E. Ahmadi, A. Aboubakri, A.K. Sadaghiani, K. Sefiane, A. Koşar, Effect of Functional Surfaces with Gradient Mixed Wettability on Flow Boiling in a High Aspect Ratio Microchannel, Fluids. 5 (2021) 5–9. https://doi.org/10.15258/sst.2020.48.1.05.
- [9] B.J. Jones, J.P. McHale, S. V. Garimella, The influence of surface roughness on nucleate pool boiling heat transfer, J. Heat Transfer. 131 (2009) 1–14. https://doi.org/10.1115/1.3220144.
- [10] A.R. Betz, J. Jenkins, C.J. Kim, D. Attinger, Boiling heat transfer on superhydrophilic, superhydrophobic, and superbiphilic surfaces, Int. J. Heat Mass Transf. 57 (2013) 733–741. https://doi.org/10.1016/J.IJHEATMASSTRANSFER.2012.10.080.
- [11] D.Y. Lim, I.C. Bang, Controlled bubble departure diameter on biphilic surfaces for enhanced pool boiling heat transfer performance, Int. J. Heat Mass Transf. 150 (2020). https://doi.org/10.1016/j.ijheatmasstransfer.2020.119360.
- [12] X. Ji, J. Xu, Z. Zhao, W. Yang, Pool boiling heat transfer on uniform and non-uniform porous coating surfaces, Exp. Therm. Fluid Sci. 48 (2013) 198–212. https://doi.org/10.1016/j.expthermflusci.2013.03.002.
- [13] M.C. Zaghdoudi, Pool Boiling Heat transfer Enhancement by Surface modification I Micro structures for Electronics cooling: A Review, 30 (2005)

- 189-212.
- [14] B. Parizad Benam, A.K. Sadaghiani, V. Yağcı, M. Parlak, K. Sefiane, A. Koşar, Review on high heat flux flow boiling of refrigerants and water for electronics cooling, Int. J. Heat Mass Transf. 180 (2021) 121787. https://doi.org/10.1016/J.IJHEATMASSTRANSFER.2021.121787.
- [15] A. Aboubakri, V.E. Ahmadi, S. Celik, A.K. Sadaghiani, K. Sefiane, A. Kosar, Effect of Surface Biphilicity on FC-72 Flow Boiling in a Rectangular Minichannel, Front. Mech. Eng. 0 (2021) 95. https://doi.org/10.3389/FMECH.2021.755580.
- [16] M.M. Rahman, S. Ridwan, D. Fehlinger, M. Mccarthy, Wicking Enhanced Critical Heat Flux for Highly Wetting Fluids on Structured Surfaces, Langmuir. 36 (2020) 9643–9648. https://doi.org/10.1021/ACS.LANGMUIR.9B03711/SUPPL_FILE/LA9B03711_ SI 003.AVI.
- [17] M. Searle, P. Emerson, J. Crockett, D. Maynes, Influence of microstructure geometry on pool boiling at superhydrophobic surfaces, Int. J. Heat Mass Transf. 127 (2018) 772–783. https://doi.org/10.1016/J.IJHEATMASSTRANSFER.2018.07.044.
- [18] B. Liu, A.I. Garivalis, Z. Cao, Y. Zhang, J. Wei, P. Di Marco, Effects of electric field on pool boiling heat transfer over microstructured surfaces under different liquid subcoolings, Int. J. Heat Mass Transf. 183 (2022) 122154. https://doi.org/10.1016/J.IJHEATMASSTRANSFER.2021.122154.
- [19] V. Serdyukov, S. Starinskiy, I. Malakhov, A. Safonov, A. Surtaev, Laser texturing of silicon surface to enhance nucleate pool boiling heat transfer, Appl. Therm. Eng. 194 (2021) 117102. https://doi.org/10.1016/J.APPLTHERMALENG.2021.117102.
- [20] J. Fernández-Seara, Á. Pardiñas, R. Diz, Heat transfer enhancement of ammonia pool boiling with an integral-fin tube, Int. J. Refrig. 69 (2016) 175–185. https://doi.org/10.1016/J.IJREFRIG.2016.05.012.
- [21] A. Jaikumar, S.G. Kandlikar, Enhanced pool boiling for electronics cooling using porous fin tops on open microchannels with FC-87, Appl. Therm. Eng. 91 (2015) 426–433.
- [22] R. Pastuszko, R. Kaniowski, T.M. Wójcik, Comparison of pool boiling performance for plain micro-fins and micro-fins with a porous layer, Appl. Therm. Eng. 166 (2020) 114658. https://doi.org/10.1016/J.APPLTHERMALENG.2019.114658.
- [23] R. Pastuszko, Pool boiling heat transfer on micro-fins with wire mesh Experiments and heat flux prediction, Int. J. Therm. Sci. 125 (2018) 197–209. https://doi.org/10.1016/j.ijthermalsci.2017.11.019.
- [24] Z. Zhao, X. Ma, S. Li, S. Yang, L. Huang, Visualization-based nucleate pool boiling heat transfer enhancement on different sizes of square micropillar array surfaces, Exp. Therm. Fluid Sci. 119 (2020) 110212. https://doi.org/10.1016/J.EXPTHERMFLUSCI.2020.110212.

- [25] J.C. Passos, R.F. Reinaldo, Analysis of pool boiling within smooth and grooved tubes, Exp. Therm. Fluid Sci. 22 (2000) 35–44.
- [26] A.K. Das, P.K. Das, P. Saha, Performance of different structured surfaces in nucleate pool boiling, Appl. Therm. Eng. 29 (2009) 3643–3653.
- [27] D. Cooke, S.G. Kandlikar, Pool Boiling Heat Transfer and Bubble Dynamics Over Plain and Enhanced Microchannels, J. Heat Transfer. 133 (2011). https://doi.org/10.1115/1.4003046.
- [28] Z.G. Xu, C.Y. Zhao, Thickness effect on pool boiling heat transfer of trapezoid-shaped copper foam fins, Appl. Therm. Eng. 60 (2013) 359–370. https://doi.org/10.1016/J.APPLTHERMALENG.2013.07.013.
- [29] D. Zhong, J. Meng, Z. Li, Z. Guo, Experimental study of saturated pool boiling from downward facing surfaces with artificial cavities, Exp. Therm. Fluid Sci. 68 (2015) 442–451. https://doi.org/10.1016/j.expthermflusci.2015.06.003.
- [30] L. Zhang, M. Shoji, Nucleation site interaction in pool boiling on the artificial surface, Int. J. Heat Mass Transf. 46 (2003) 513–522. https://doi.org/10.1016/S0017-9310(02)00291-0.
- [31] C.K. Yu, D.C. Lu, T.C. Cheng, Pool boiling heat transfer on artificial microcavity surfaces in dielectric fluid FC-72, J. Micromechanics Microengineering. 16 (2006) 2092–2099. https://doi.org/10.1088/0960-1317/16/10/024.
- [32] P.H. Lin, B.R. Fu, C. Pan, Critical heat flux on flow boiling of methanol—water mixtures in a diverging microchannel with artificial cavities, Int. J. Heat Mass Transf. 54 (2011) 3156–3166. https://doi.org/10.1016/J.IJHEATMASSTRANSFER.2011.04.016.
- [33] C. Hutter, D.B.R. Kenning, K. Sefiane, T.G. Karayiannis, H. Lin, G. Cummins, A.J. Walton, Experimental pool boiling investigations of FC-72 on silicon with artificial cavities and integrated temperature microsensors, Exp. Therm. Fluid Sci. 34 (n.d.) 422–433. https://doi.org/10.1016/j.expthermflusci.2009.03.010.
- [34] A. Sitar, M. Može, M. Crivellari, J. Schille, I. Golobič, Nucleate pool boiling heat transfer on etched and laser structured silicon surfaces, Int. J. Heat Mass Transf. 147 (2020) 118956. https://doi.org/10.1016/J.IJHEATMASSTRANSFER.2019.118956.
- [35] G. Chen, M. Jia, S. Zhang, Y. Tang, Z. Wan, Pool boiling enhancement of novel interconnected microchannels with reentrant cavities for high-power electronics cooling, Int. J. Heat Mass Transf. 156 (2020) 119836. https://doi.org/10.1016/J.IJHEATMASSTRANSFER.2020.119836.
- [36] W. Hao, T. Wang, Y. yan Jiang, C. Guo, C. hong Guo, Pool boiling heat transfer on deformable structures made of shape-memory-alloys, Int. J. Heat Mass Transf. 112 (2017) 236–247. https://doi.org/10.1016/J.IJHEATMASSTRANSFER.2017.04.113.
- [37] W.T. Ji, C.Y. Zhao, D.C. Zhang, P.F. Zhao, Z.Y. Li, Y.L. He, W.Q. Tao, Pool boiling heat transfer of R134a outside reentrant cavity tubes at higher heat flux, Appl. Therm. Eng. 127 (2017) 1364–1371. https://doi.org/10.1016/J.APPLTHERMALENG.2017.08.130.

- [38] J.P. McHale, S. V Garimella, Nucleate boiling from smooth and rough surfaces—Part 1: Fabrication and characterization of an optically transparent heater—sensor substrate with controlled surface roughness, Exp. Therm. Fluid Sci. 44 (2013) 456–467.
- [39] J.P. McHale, S. V. Garimella, Nucleate boiling from smooth and rough surfaces Part 2: Analysis of surface roughness effects on nucleate boiling, Exp. Therm. Fluid Sci. 44 (2013) 439–455. https://doi.org/10.1016/J.EXPTHERMFLUSCI.2012.08.005.
- [40] J.E. BENJAMIN, Bubble growth in nucleate boiling of a binary mixture, Univ. Illinois. (1960).
- [41] L. Dong, X. Quan, P. Cheng, An analysis of surface-microstructures effects on heterogeneous nucleation in pool boiling, Int. J. Heat Mass Transf. 55 (2012) 4376–4384. https://doi.org/10.1016/J.IJHEATMASSTRANSFER.2012.04.006.
- [42] L. Dong, X. Quan, P. Cheng, An experimental investigation of enhanced pool boiling heat transfer from surfaces with micro/nano-structures, Int. J. Heat Mass Transf. 71 (2014) 189–196. https://doi.org/10.1016/J.IJHEATMASSTRANSFER.2013.11.068.
- [43] I. Mudawar, T.M. Anderson, Parametric Investigation Into the Effects of Pressure, Subcooling, Surface Augmentation and Choice of Coolant on Pool Boiling in the Design of Cooling Systems for High-Power-Density Electronic Chips, J. Electron. Packag. 112 (1990) 375–382. https://doi.org/10.1115/1.2904392.
- [44] T.M. Anderson, I. Mudawar, Microelectronic cooling by enhanced pool boiling of a dielectric fluorocarbon liquid, J. Heat Transfer. 111 (1989) 752–759. https://doi.org/10.1115/1.3250747.
- [45] G. Liang, I. Mudawar, Review of pool boiling enhancement by surface modification, Int. J. Heat Mass Transf. 128 (2019) 892–933. https://doi.org/10.1016/j.ijheatmasstransfer.2018.09.026.
- [46] T. Li, X. Wu, Q. Ma, Pool boiling heat transfer of R141b on surfaces covered copper foam with circular-shaped channels, Exp. Therm. Fluid Sci. 105 (2019) 136–143. https://doi.org/10.1016/j.expthermflusci.2019.03.015.
- [47] C.K. Yu, D.C. Lu, Pool boiling heat transfer on horizontal rectangular fin array in saturated FC-72, Int. J. Heat Mass Transf. 50 (2007) 3624–3637.
- [48] M. Zupančič, M. Steinbücher, P. Gregorčič, I. Golobič, Enhanced pool-boiling heat transfer on laser-made hydrophobic/superhydrophilic polydimethylsiloxanesilica patterned surfaces, Appl. Therm. Eng. 91 (2015) 288–297.
- [49] S. Chatpun, M. Watanabe, M. Shoji, Experimental study on characteristics of nucleate pool boiling by the effects of cavity arrangement, Exp. Therm. Fluid Sci. 29 (2004) 33–40. https://doi.org/10.1016/J.EXPTHERMFLUSCI.2004.01.007.
- [50] A. Nikulin, J.L. Dauvergne, A. Ortuondo, E.P. del Barrio, Spacing effect on pool boiling performance of three triangular pitched and vertically oriented tubes, Int. Commun. Heat Mass Transf. 126 (2021) 105452. https://doi.org/10.1016/J.ICHEATMASSTRANSFER.2021.105452.

- [51] M. Kole, S. Khandekar, Engineering applications of ferrofluids: A review, J. Magn. Magn. Mater. 537 (2021) 168222. https://doi.org/10.1016/j.jmmm.2021.168222.
- [52] X. Fang, Y. Chen, H. Zhang, W. Chen, A. Dong, R. Wang, Heat transfer and critical heat flux of nanofluid boiling: A comprehensive review, Renew. Sustain. Energy Rev. 62 (2016) 924–940. https://doi.org/10.1016/J.RSER.2016.05.047.
- [53] Y. Şişman, A.K. Sadaghiani, K.R. Khedir, M. Brozak, T. Karabacak, A. Koşar, Subcooled Flow Boiling Over Microstructured Plates In Rectangular Minichannels, Nanoscale Microscale Thermophys. Eng. 20 (2016) 173–190. https://doi.org/10.1080/15567265.2016.1248584.
- [54] A.E. Bergles, Enhancement of pool boiling, Int. J. Refrig. 20 (1997) 545–551. https://doi.org/10.1016/S0140-7007(97)00063-7.
- [55] M. Saedi, H. Aminfar, M. Mohammadpourfard, R. Maroofiazar, Simulation of ferrofluid flow boiling in helical tubes using two-fluid model, Heat Mass Transf. Und Stoffuebertragung. 55 (2019) 1–16. https://doi.org/10.1007/S00231-018-2400-9/FIGURES/21.
- [56] X. Fang, R. Wang, W. Chen, H. Zhang, C. Ma, A review of flow boiling heat transfer of nanofluids, Appl. Therm. Eng. 91 (2015) 1003–1017. https://doi.org/10.1016/J.APPLTHERMALENG.2015.08.100.
- [57] K.C. Leong, J.Y. Ho, K.K. Wong, A critical review of pool and flow boiling heat transfer of dielectric fluids on enhanced surfaces, Appl. Therm. Eng. 112 (2017) 999–1019. https://doi.org/10.1016/J.APPLTHERMALENG.2016.10.138.
- [58] A. Ateş, B. Parizad Benam, V. Yağcı, M. Çağlar Malyemez, M. Parlak, A.K. Sadaghiani, A. Koşar, On the effect of elliptical pin Fins, distribution pin Fins, and tip clearance on the performance of heat sinks in flow boiling, Appl. Therm. Eng. 212 (2022) 118648. https://doi.org/10.1016/J.APPLTHERMALENG.2022.118648.
- [59] H. Aminfar, M. Mohammadpourfard, S.A. Zonouzi, Numerical investigation of the transient hydrothermal behavior a ferrofluid flowing through a helical duct in the presence of nonuniform magnetic field, J. Heat Transfer. 136 (2014). https://doi.org/10.1115/1.4026487/372615.
- [60] M. Mohammadpourfard, H. Aminfar, S. Ahangar Zonouzi, Numerical Investigation of the Magnetic Field Effects on the Entropy Generation and Heat Transfer in a Nanofluid Filled Cavity with Natural Convection, Heat Transf. Res. 46 (2017) 409–433. https://doi.org/10.1002/HTJ.21222.
- [61] R. Hiergeist, W. Andrä, N. Buske, R. Hergta, I. Hilger, U. Richter, W. Kaiser, Application of magnetite ferrofluids for hyperthermia, J. Magn. Magn. Mater. 201 (1999) 420–422. https://doi.org/10.1016/S0304-8853(99)00145-6.
- [62] I. Torres-Díaz, C. Rinaldi, Recent progress in ferrofluids research: Novel applications of magnetically controllable and tunable fluids, Soft Matter. 10 (2014) 8584–8602. https://doi.org/10.1039/C4SM01308E.
- [63] C. Scherer, A.M. Figueiredo Neto, Ferrofluids: properties and applications, Brazilian J. Phys. 35 (2005) 718–727. https://doi.org/10.1590/S0103-

- 97332005000400018.
- [64] M.H. Taheri, M. Mohammadpourfard, A.K. Sadaghiani, A. Kosar, Wettability alterations and magnetic field effects on the nucleation of magnetic nanofluids: A molecular dynamics simulation, J. Mol. Liq. 260 (2018) 209–220. https://doi.org/10.1016/j.molliq.2018.03.075.
- [65] S. Ahangar Zonouzi, H. Aminfar, M. Mohammadpourfard, A review on effects of magnetic fields and electric fields on boiling heat transfer and CHF, Appl. Therm. Eng. 151 (2019) 11–25. https://doi.org/10.1016/j.applthermaleng.2019.01.099.
- [66] E. Raki, M. Afrand, A. Abdollahi, Influence of magnetic field on boiling heat transfer coefficient of a magnetic nanofluid consisting of cobalt oxide and deionized water in nucleate regime: An experimental study, Int. J. Heat Mass Transf. 165 (2021) 120669. https://doi.org/10.1016/j.ijheatmasstransfer.2020.120669.
- [67] Y.W. Lee, T.L. Chang, Novel perturbations between magnetic nanofluid and the thermal fluidic system at heat dissipation, Microelectron. Eng. 111 (2013) 58–63. https://doi.org/10.1016/J.MEE.2013.01.048.
- [68] A. Miaskowski, B. Sawicki, Magnetic fluid hyperthermia modeling based on phantom measurements and realistic breast model, IEEE Trans. Biomed. Eng. 60 (2013) 1806–1813. https://doi.org/10.1109/TBME.2013.2242071.
- [69] M. Lin, D. Zhang, J. Huang, J. Zhang, W. Xiao, H. Yu, L. Zhang, J. Ye, The anti-hepatoma effect of nanosized Mn–Zn ferrite magnetic fluid hyperthermia associated with radiation in vitro and in vivo, Nanotechnology. 24 (2013) 255101. https://doi.org/10.1088/0957-4484/24/25/255101.
- [70] A.K. Sadaghiani, A. Kos, International Journal of Heat and Mass Transfer Numerical and experimental investigation on the effects of diameter and length on high mass flux subcooled flow boiling in horizontal microtubes, 92 (2016) 824–837. https://doi.org/10.1016/j.ijheatmasstransfer.2015.09.004.
- [71] H. Jafari Zandabad, L. Jahanshaloo, H. Aminfar, M. Mohammadpourfard, Experimental study of the effects of quadrupole magnetic field and hydro-thermal parameters on bubble departure diameter and frequency in a vertical annulus, Exp. Heat Transf. 00 (2021) 1–28. https://doi.org/10.1080/08916152.2021.1873877.
- [72] A.K. Sadaghiani, H. Rajabnia, S. Çelik, H. Noh, H.J. Kwak, M. Nejatpour, H.S. Park, H.Y. Acar, B. Mısırlıoğlu, M.R. Özdemir, A. Koşar, Pool boiling heat transfer of ferrofluids on structured hydrophilic and hydrophobic surfaces: The effect of magnetic field, Int. J. Therm. Sci. 155 (2020). https://doi.org/10.1016/j.ijthermalsci.2020.106420.
- [73] M. Şeşen, Y. Tekşen, K. Şendur, M. Pinar Mengüç, H. Öztürk, H.F. Yağc Acar, A. Koşar, Heat transfer enhancement with actuation of magnetic nanoparticles suspended in a base fluid, J. Appl. Phys. 112 (2012) 064320. https://doi.org/10.1063/1.4752729.
- [74] M.M. Sarafraz, S.M. Peyghambarzadeh, Experimental study on subcooled flow boiling heat transfer to water–diethylene glycol mixtures as a coolant inside a

- vertical annulus, Exp. Therm. Fluid Sci. 50 (2013) 154–162. https://doi.org/10.1016/J.EXPTHERMFLUSCI.2013.06.003.
- [75] S. Ahangar Zonouzi, R. Khodabandeh, H. Safarzadeh, H. Aminfar, Y. Trushkina, M. Mohammadpourfard, M. Ghanbarpour, G. Salazar Alvarez, Experimental investigation of the flow and heat transfer of magnetic nanofluid in a vertical tube in the presence of magnetic quadrupole field, Exp. Therm. Fluid Sci. 91 (2018) 155–165. https://doi.org/10.1016/J.EXPTHERMFLUSCI.2017.10.013.
- [76] M. Lajvardi, J. Moghimi-Rad, I. Hadi, A. Gavili, T. Dallali Isfahani, F. Zabihi, J. Sabbaghzadeh, Experimental investigation for enhanced ferrofluid heat transfer under magnetic field effect, J. Magn. Magn. Mater. 322 (2010) 3508–3513. https://doi.org/10.1016/J.JMMM.2010.06.054.
- [77] K. Guo, H. Li, Y. Feng, T. Wang, J. Zhao, Enhancement of non-uniform magnetic field on saturated film boiling of magnetic nanofluid (MNF), Int. J. Heat Mass Transf. 143 (2019) 118594. https://doi.org/10.1016/J.IJHEATMASSTRANSFER.2019.118594.
- [78] K. Guo, H. Li, Y. Feng, T. Wang, J. Zhao, Numerical simulation of magnetic nanofluid (MNF) film boiling using the VOSET method in presence of a uniform magnetic field, Int. J. Heat Mass Transf. 134 (2019) 17–29. https://doi.org/10.1016/J.IJHEATMASSTRANSFER.2018.12.148.
- [79] H. Arya, M.M. Sarafraz, M. Arjomandi, Pool boiling under the magnetic environment: experimental study on the role of magnetism in particulate fouling and bubbling of iron oxide/ethylene glycol nano-suspension, Heat Mass Transf. Und Stoffuebertragung. 55 (2019) 119–132. https://doi.org/10.1007/S00231-018-2438-8/FIGURES/11.
- [80] H. Aminfar, M. Mohammadpourfard, F. Mohseni, Two-phase mixture model simulation of the hydro-thermal behavior of an electrical conductive ferrofluid in the presence of magnetic fields, J. Magn. Magn. Mater. 324 (2012) 830–842. https://doi.org/10.1016/J.JMMM.2011.09.028.
- [81] A. Ghofrani, M.H. Dibaei, A. Hakim Sima, M.B. Shafii, Experimental investigation on laminar forced convection heat transfer of ferrofluids under an alternating magnetic field, Exp. Therm. Fluid Sci. 49 (2013) 193–200. https://doi.org/10.1016/J.EXPTHERMFLUSCI.2013.04.018.
- [82] H. Andersson, W. Van Der Wijngaart, P. Nilsson, P. Enoksson, G. Stemme, A valve-less diffuser micropump for microfluidic analytical systems, Sensors Actuators B Chem. 72 (2001) 259–265. https://doi.org/10.1016/S0925-4005(00)00644-4.
- [83] D.-H. Ha, V.P. Phan, N.S. Goo, C.H. Han, Three-dimensional electro-fluid–structural interaction simulation for pumping performanceevaluation of a valveless micropump, Smart Mater. Struct. 18 (2009) 104015. https://doi.org/10.1088/0964-1726/18/10/104015.
- [84] H. Coleman, W. Steck, Experimentation, validation, and uncertainty analysis for engineers, Prentice-Hall, Inc, 2018.
- [85] H.R. Cho, S.C. Park, D. Kim, H.M. Joo, D.I. Yu, Experimental study on pool boiling on hydrophilic micro/nanotextured surfaces with hydrophobic patterns,

- Energies. 14 (2021) 1–13. https://doi.org/10.3390/en14227543.
- [86] P. KC, A. Nammari, T.S. Ashton, A.L. Moore, Saturated pool boiling heat transfer from vertically oriented silicon surfaces modified with foam-like hexagonal boron nitride nanomaterials, Int. J. Heat Mass Transf. 95 (2016) 964–971. https://doi.org/10.1016/j.ijheatmasstransfer.2016.01.006.
- [87] B. Liu, J. Liu, Y. Zhang, J. Wei, W. Wang, Experimental and theoretical study of pool boiling heat transfer and its CHF mechanism on femtosecond laser processed surfaces, Int. J. Heat Mass Transf. 132 (2019) 259–270. https://doi.org/10.1016/j.ijheatmasstransfer.2018.12.003.
- [88] A. Jaikumar, S.G. Kandlikar, Ultra-high pool boiling performance and effect of channel width with selectively coated open microchannels, Int. J. Heat Mass Transf. 95 (2016) 795–805. https://doi.org/10.1016/j.ijheatmasstransfer.2015.12.061.
- [89] G. Liang, Y. Chen, H. Yang, D. Li, S. Shen, Nucleate boiling heat transfer and critical heat flux (CHF) from micro-pit surfaces, Int. J. Heat Mass Transf. 152 (2020) 119510. https://doi.org/10.1016/j.ijheatmasstransfer.2020.119510.
- [90] A. Jaikumar, S.G. Kandlikar, microchannels Pool boiling enhancement through bubble induced convective liquid flow in feeder microchannels, 041604 (2017). https://doi.org/10.1063/1.4941032.
- [91] G. Liang, I. Mudawar, Pool boiling critical heat flux (CHF) Part 1: Review of mechanisms, models, and correlations, Int. J. Heat Mass Transf. 117 (2018) 1352–1367. https://doi.org/10.1016/j.ijheatmasstransfer.2017.09.134.
- [92] N. Zuber, M. Tribus, Further remarks on the stability of boiling heat transfer. Report 58-5, (1958). https://doi.org/10.2172/4332326.
- [93] Y. Haramura, Y. Katto, A new hydrodynamic model of critical heat flux, applicable widely to both pool and forced convection boiling on submerged bodies in saturated liquids, J. Heat Mass Transf. 26 (1983) 389–399.
- [94] J.F. Klausner, R. Mei, D.M. Bernhard, L.Z. Zeng, Vapor bubble departure in forced convection boiling, Int. J. Heat Mass Transf. 36 (1993) 651–662. https://doi.org/10.1016/0017-9310(93)80041-R.
- [95] R. Mei, J.F. Klausner, Shear lift force on spherical bubbles, Int. J. Heat Fluid Flow. 15 (1994) 62–65. https://doi.org/10.1016/0142-727X(94)90031-0.
- [96] R. Chen, Y., Groll, M., Mertz, R., Kulenovic, Force analysisi for isolated bubbles growing from smooth and evaporator tubes, (2003).
- [97] N. Zuber, The dynamics of vapor bubbles in nonuniform temperature fields, Int. J. Heat Mass Transf. 2 (1961) 83–98. https://doi.org/10.1016/0017-9310(61)90016-3.
- [98] Q.A. Pankhurst, J. Connolly, S.K. Jones, J. Dobson, Applications of magnetic nanoparticles in biomedicine, J. Phys. D. Appl. Phys. 36 (2003) R167. https://doi.org/10.1088/0022-3727/36/13/201.
- [99] H. Aminfar, M. Mohammadpourfard, R. Maroofiazar, Experimental study on the effect of magnetic field on critical heat flux of ferrofluid flow boiling in a vertical

- annulus, Exp. Therm. Fluid Sci. 58 (2014) 156–169. https://doi.org/10.1016/j.expthermflusci.2014.06.023.
- [100] Magnetic field of two Helmholtz coils, (n.d.). https://virtuelle-experimente.de/en/b-feld/b-feld/helmholtzspulenpaar.php (accessed June 16, 2022).
- [101] R. Shah, A. London, Laminar flow forced convection in ducts: a source book for compact heat exchanger analytical data, 2014.